Available online at www.sciencedirect.com
ScienceDirect
Comput. Methods Appl. Mech. Engrg. 285 (2015) 32–63
Computer methods in applied mechanics and engineering
www.elsevier.com/locate/cma

Assessment of variational multiscale models for the large eddy simulation of turbulent incompressible flows

Oriol Colomés[a], Santiago Badia[c,a], Ramon Codina[c,b], Javier Principe[d,a,*]

[a] *Centre Internacional de Mètodes Numèrics en Enginyeria (CIMNE), Parc Mediterrani de la Tecnologia, UPC, Esteve Terradas 5, 08860 Castelldefels, Spain*
[b] *Centre Internacional de Mètodes Numèrics en Enginyeria (CIMNE), Jordi Girona 1-3, Campus Nord UPC, Edifici C1, 08034 Barcelona, Spain*
[c] *Universitat Politècnica de Catalunya Jordi Girona 1-3, Campus Nord UPC, Edifici C1, 08034 Barcelona, Spain*
[d] *Universitat Politècnica de Catalunya, Urgell 187, 08036 Barcelona, Spain*

Received 19 November 2013; received in revised form 24 October 2014; accepted 25 October 2014
Available online 11 November 2014

Abstract

In this work we study the performance of some variational multiscale models (VMS) in the large eddy simulation (LES) of turbulent flows. We consider VMS models obtained by different subgrid scale approximations which include either static or dynamic subscales, linear or nonlinear multiscale splitting, and different choices of the subscale space. After a brief review of these models, we discuss some implementation aspects particularly relevant to the simulation of turbulent flows, namely the use of a skew symmetric form of the convective term and the computation of projections when orthogonal subscales are used. We analyze the energy conservation (and numerical dissipation) of the alternative VMS formulations, which is numerically evaluated. In the numerical study, we have considered three well known problems: the decay of homogeneous isotropic turbulence, the Taylor–Green vortex problem and the turbulent flow in a channel. We compare the results obtained using different VMS models, paying special attention to the effect of using orthogonal subscale spaces. The VMS results are also compared against classical LES scheme based on filtering and the dynamic Smagorinsky closure. Altogether, our results show the tremendous potential of VMS for the numerical simulation of turbulence. Further, we study the sensitivity of VMS to the algorithmic constants and analyze the behavior in the small time step limit. We have also carried out a computational cost comparison of the different formulations. Out of these experiments, we can state that the numerical results obtained with the different VMS formulations (as far as they converge) are quite similar. However, some choices are prone to instabilities and the results obtained in terms of computational cost are certainly different. The dynamic orthogonal subscales model turns out to be best in terms of efficiency and robustness.

Keywords: Turbulence; Large eddy simulation; Stabilization; Variational multiscale

* Corresponding author at: Universitat Politècnica de Catalunya, Urgell 187, 08036 Barcelona, Spain.
E-mail addresses: ocolomes@cimne.upc.edu (O. Colomés), sbadia@cimne.upc.edu (S. Badia), ramon.codina@upc.edu (R. Codina), principe@cimne.upc.edu (J. Principe).

http://dx.doi.org/10.1016/j.cma.2014.10.041
0045-7825/

1. Introduction

LES techniques for the numerical simulation of turbulent flows [1] are based on a scale separation that permits to reduce the computational cost with respect to direct numerical simulation (DNS). Such scale separation is traditionally achieved by filtering the original Navier–Stokes equations, which leads to an extra forcing term defined by a physical (functional or structural) model. This widely used approach is usually referred to as explicit LES [1].

By contrast, implicit LES techniques (ILES) rely on purely numerical artifacts without any modification of the continuous problem. This approach was seldom followed, the MILES (Monotone Integrated LES) approach [2–4] being the main exception, until the VMS method was introduced [5,6] and subsequently proposed as an ILES method (see below). ILES techniques are usually considered to be based on the addition of purely dissipative numerical terms, see [1, Section 5.3.4]. It is worth emphasizing that this is not the case of some particular VMS models, as it is shown in [7] and discussed below.

VMS was introduced in [5,6] as a framework for the motivation and development of stabilization techniques, which aim to overcome numerical difficulties encountered when using the standard Galerkin method. On the one hand, the velocity and pressure finite element (FE) spaces need to satisfy the *inf–sup* compatibility condition that guarantees pressure stability and precludes the use of equal order interpolation. Mixed methods satisfying this condition can be used and their finite volume counterpart, based on staggered grids, are common in the LES community. Stabilization techniques that permit the use of equal order interpolation were proposed, e.g., in [8,9]. On the other hand, global nonphysical oscillations appear in the convection dominated regime, when the mesh is not fine enough, that is, for high mesh Reynolds number flows. The only way to overcome this problem is through the addition of some form of dissipation which was recognized in the early development of stabilized methods [10]. Let us note that the common practice in the LES community is to rely on the explicit extra term introduced by the physical model using high order approximations of the convective term.[1]

The first attempts to perform LES using VMS concepts, presented in [11–15], were performed introducing explicit subgrid modeling. The VMS models used in these works split resolved scales into large and small, introducing an explicit LES model to account for the small scales stress tensor, e.g., a Smagorinsky-type dissipative term acting on the small scales only. As a result, an important fraction of the degrees of freedom is used for the small resolved scales whereas consistency is retained in the large resolved scales only.

ILES using a VMS approach with resolved and unresolved subgrid scales (the setting that permits to recover stabilized formulations) was suggested in [16] and performed in [17–19]. Excellent results were first presented in [18], but using isogeometric analysis for the space approximation [20]. Compared to classical LES based on filtering, the VMS approach does not face difficulties associated to inhomogeneous non-commutative filters in wall-bounded flows. Further, it retains numerical consistency in the FE equations and optimal convergence up to the interpolation order whereas, e.g., Smagorinsky models introduce a consistency error of order $h^{4/3}$ (see [11,12,18]).

Scale separation is achieved in the VMS formalism by a variational projection. The continuous unknown is split into a resolvable FE component and an unresolvable subgrid or subscale component. The action of the subscales onto the FE scales can be approximated in different ways, leading to different VMS models but in all cases these models are *residual based* (no eddy viscosity is introduced), which permits to retain consistency. Among the modeling possibilities is the choice of the subscale space, first discussed in [21], where it was enforced to be L^2-orthogonal to the FE space. Another modeling ingredient is the possibility of considering time-dependent subscales and to keep the VMS decomposition in all the nonlinear terms, which was studied in [16,22]. Clear improvements have been observed when using dynamic and fully nonlinear models for the simulation of laminar flows [22,23].

In this work we assess implicit VMS models for the numerical simulation of turbulent flows. We refer to the original references for a comprehensive treatment of the assumptions of the formulations and their numerical analysis. Our intention here is to compare the different VMS schemes in terms of quality of the results and computational cost, and discuss some implementation aspects that we find particularly relevant for the simulation of turbulent flows. Our main motivation is to compare the influence of using orthogonal subscales, in order to enrich current comparisons on VMS techniques for large-eddy simulations, such as [24], where only non-projected subscales are considered. We

[1] It is worth pointing out that both problems (convection instability and compatibility conditions) are also present in the *linear* Oseen problem. One of the inconsistencies of an explicit LES approach without a numerical dissipation term is that convection is stabilized by a term that comes from the physical model of the nonlinear Navier–Stokes equations and such a term is not present when the linear Oseen problem is considered.

present a detailed numerical experimentation for three well known problems: the decay of homogeneous isotropic turbulence (DHIT), the Taylor–Green vortex (TGV) and the turbulent flow in a channel (TCF). Thus, both unbounded and wall-bounded flows are considered; only wall-bounded tests are performed in [24]. Some other differences with respect to [24] are: (1) we consider a nonlinear sub-scale equation; (2) we do not include the time step size in the stabilization term; (3) we have analyzed the effect of the skew-symmetric term.

The first implementation aspect we discuss is the treatment of the convective term. As it is well-known, the numerical analysis [25–27] requires a skew-symmetric form of this term in order to avoid any positive contribution to the energy estimates that cannot be properly controlled. The construction of numerical schemes that preserve the skew-symmetry of the convective term at the discrete level has been long studied in the finite difference and finite volume contexts [28–33]. However, FE formulations used to perform VMS-based LES use either the conservative form [11,14,17,18,24,34–36] or the non-conservative one [7,15,22]. The approach we follow here is similar to that in [37] and is based on a split of the convective term into conservative and non-conservative terms. In the FE (variational) context, this simple approach guarantees the preservation of skew-symmetry at the discrete level. We remark that in the nonlinear VMS models the convective velocity is discontinuous (due to the subscale contribution), which prevents us to use some popular skewsymmetric forms. We also show numerically that a positive energy contribution actually appears if a non skew-symmetric form is used.

The second point that we address is the use of weighted (by the stabilization parameter) projections and consistent mass matrices when orthogonal subscales are considered. Even though it is cheaper to use non-weighted projections and lumped mass matrices, only the use of consistent projections guarantees exact L^2 orthogonality. An alternative is the use of Scott–Zhang projections recently proposed in [38], although we do not consider this approach here.

We also discuss the influence of the algorithmic constants of the stabilization parameters in the numerical results. In particular, we show that the choice of the stabilization parameter multiplying the div–div term has a strong influence on the numerical results while it is not essential for stability and convergence of the methods. We further analyze the behavior of the VMS formulation as the time step size is reduced. These two facts are actually related by the way the stabilization parameters are usually defined (see [24,39]).

Finally, we compare the results obtained using VMS models against those obtained using classical LES based on filtering and the dynamic Smagorinsky closure [40], and another implicit LES method, the adaptive local deconvolution presented in [41].

The article is organized as follows. In Section 2 we present the VMS formulation, how to compute truly orthogonal subscales and the different models we aim at analyzing, whereas in Section 3 we discuss energy conservation statements and how they are influenced by the choice of the VMS method and the definition of the convective term. Sections 5–7 are devoted to the numerical approximation of the DHIT, the TGV, and the TCF problems, respectively. Sections 8 and 9 discuss the effect of the algorithmic constants on the results and the behavior of the different schemes in the small time step limit. Some remarks close the article in Section 10.

2. Formulation

2.1. Navier–Stokes problem

Let Ω be a bounded domain of $\mathbb{R}^d$, where $d = 2, 3$ is the number of space dimensions, $\Gamma = \partial\Omega$ its boundary and $[0, T]$ the time interval. The strong form of the incompressible Navier–Stokes problem consists of finding the velocity field $\mathbf{u}$ and the pressure field p such that

$$\partial_t \mathbf{u} - \nu\Delta\mathbf{u} + \mathbf{u}\cdot\nabla\mathbf{u} + \nabla p = \mathbf{f} \quad \text{in } \Omega\times(0,T), \tag{1}$$

$$\nabla\cdot\mathbf{u} = 0 \quad \text{in } \Omega\times(0,T), \tag{2}$$

with $\mathbf{f}$ the force vector and ν the kinematic viscosity. Hereinafter bold characters denote vectors and tensors.

Eqs. (1)–(2) have to be supplied with appropriate boundary and initial conditions. The boundary Γ is divided into the Dirichlet (Γ_D) and the Neumann (Γ_N) parts such that $\Gamma_D \cup \Gamma_N = \Gamma$ and $\Gamma_D \cap \Gamma_N = \emptyset$. Then, the boundary and initial conditions can be written as

$$\mathbf{u} = \mathbf{u}_g \quad \text{on } \Gamma_D\times(0,T], \tag{3}$$

$$(-p\mathbf{I} + \nu(\nabla\mathbf{u} + \nabla\mathbf{u}^T))\cdot\mathbf{n} = \mathbf{t}_N \quad \text{on } \Gamma_N\times(0,T], \tag{4}$$

$$\mathbf{u}(\mathbf{x}, 0) = \mathbf{u}_0(\mathbf{x}) \quad \text{in } \Omega \times \{0\}, \tag{5}$$

$\mathbf{n}$ being the unit outward vector normal to Γ. To simplify the exposition, we will consider $\mathbf{u}_g = \mathbf{0}$ and $\Gamma_D = \Gamma$ in what follows.

In order to derive the weak form of the problem (1)–(5) we define some notation that will be used hereafter. We denote by $L^p(\Omega)$, $1 \leq p < \infty$, the spaces of functions such that their pth power is absolutely integrable in Ω. For the case in which $p = 2$, we have a Hilbert space with scalar product

$$(u, v)_\Omega \equiv (u, v) := \int_\Omega u(\mathbf{x})\, v(\mathbf{x}) d\Omega \tag{6}$$

and induced norm $\|u\|_{L^2(\Omega)} \equiv \|u\| = (u, u)^{1/2}$. Abusing of the notation, the same symbol as in (6) will be used for the integral of the product of two functions, even if these are not in $L^2(\Omega)$, and both for scalar and vector fields. The space of functions whose distributional derivatives up to order m are in $L^2(\Omega)$ are denoted by $H^m(\Omega)$. We will focus on the case of $m = 1$, which is also a Hilbert space. $H_0^1(\Omega)$ is the set of functions in $H^1(\Omega)$ that have zero trace on Γ. Furthermore, we denote by $H^{-1}(\Omega)$ the topological dual of $H_0^1(\Omega)$ and by $\langle \cdot, \cdot \rangle$ the duality pairing between $H^{-1}(\Omega)$ and $H_0^1(\Omega)$. Given a Banach space X, $L^p(0, T; X)$ is the space of time dependent functions such that their X-norm is in $L^p(0, T)$.

The weak form of the incompressible Navier–Stokes problem (1)–(5) consists, e.g., in finding $[\mathbf{u}, p] \in L^2(0, T; \mathcal{V}_0) \times \mathcal{D}'(0, T; \mathcal{Q}_0)$ (distributions in time with values in $\mathcal{Q}_0$) such that

$$(\partial_t \mathbf{u}, \mathbf{v}) + B(\mathbf{u}; [\mathbf{u}, p], [\mathbf{v}, q]) = \langle \mathbf{f}, \mathbf{v} \rangle \quad \forall \mathbf{v} \in \mathcal{V}_0,\ \forall q \in \mathcal{Q}_0, \tag{7}$$

satisfying the initial condition (5) in a weak sense. Here $\mathcal{V}_0 := H_0^1(\Omega)^d$, $\mathcal{Q}_0 := L^2(\Omega)/\mathbb{R}$ and the form $B(\mathbf{a}; [\mathbf{u}, p], (\mathbf{v}, q))$ is defined as

$$B(\mathbf{a}; [\mathbf{u}, p], [\mathbf{v}, q]) := \nu(\nabla \mathbf{u}, \nabla \mathbf{v}) + b(\mathbf{a}, \mathbf{u}, \mathbf{v}) - (p, \nabla \cdot \mathbf{v}) + (q, \nabla \cdot \mathbf{u}) \tag{8}$$

where the trilinear weak form of the convective term $b(\mathbf{u}, \mathbf{v}, \mathbf{w})$ can be written in the following three equivalent ways

$$b(\mathbf{u}, \mathbf{v}, \mathbf{w}) = (\mathbf{u} \cdot \nabla \mathbf{v}, \mathbf{w}) \quad \text{Non conservative}, \tag{9}$$

$$b(\mathbf{u}, \mathbf{v}, \mathbf{w}) = \frac{1}{2}(\mathbf{u} \cdot \nabla \mathbf{v}, \mathbf{w}) - \frac{1}{2}(\mathbf{v}, \mathbf{u} \cdot \nabla \mathbf{w}) \quad \text{Skew-symmetric (type 1)}, \tag{10}$$

$$b(\mathbf{u}, \mathbf{v}, \mathbf{w}) = (\mathbf{u} \cdot \nabla \mathbf{v}, \mathbf{w}) + \frac{1}{2}(\mathbf{v} \cdot \mathbf{w}, \nabla \cdot \mathbf{u}) \quad \text{Skew-symmetric (type 2)}. \tag{11}$$

This equivalence is lost at the discrete level. The skew-symmetric form (type 2) (11) is very common when numerical analysis are presented [25–27] but the skew-symmetric form (type 2) (10) has important advantages when the first argument is a discontinuous function, as will be shown below.

2.2. VMS framework

Let us consider a FE partition $\mathcal{T}_h$ of the domain Ω from which we can construct conforming finite dimensional spaces for the velocity $\mathcal{V}_{0,h} \subset \mathcal{V}_0$, and for the pressure $\mathcal{Q}_{0,h} \subset \mathcal{Q}_0$.

The Galerkin FE approximation of (7) consists in finding $[\mathbf{u}_h, p_h] \in L^2(0, T; \mathcal{V}_{0,h}) \times \mathcal{D}'(0, T; \mathcal{Q}_{0,h})$ such that

$$(\partial_t \mathbf{u}_h, \mathbf{v}_h) + B(\mathbf{u}_h; [\mathbf{u}_h, p_h], [\mathbf{v}_h, q_h]) = \langle \mathbf{f}, \mathbf{v}_h \rangle \quad \forall \mathbf{v}_h \in \mathcal{V}_{0,h}, \forall q_h \in \mathcal{Q}_{0,h}. \tag{12}$$

It is well known that (12) has numerical instabilities for high mesh Reynolds number problems, i.e., when the nonlinear convective term dominates the viscous term. Another drawback of that formulation is the discrete *inf–sup* condition that must be satisfied by the pair $\mathcal{V}_{0,h} \times \mathcal{Q}_{0,h}$ in order to have a well-posed problem with bounded pressure. These difficulties are overcome by using the VMS approach that follows.

Let us consider a two-scale decomposition of spaces $\mathcal{V}_0$ and $\mathcal{Q}_0$ such that $\mathcal{V}_0 = \mathcal{V}_{0,h} \oplus \widetilde{\mathcal{V}}_0$ and $\mathcal{Q} = \mathcal{Q}_{0,h} \oplus \widetilde{\mathcal{Q}}_0$, where $\widetilde{\mathcal{V}}_0$ and $\widetilde{\mathcal{Q}}_0$ are infinite-dimensional spaces that complete the FE spaces in $\mathcal{V}_0$ and $\mathcal{Q}_0$, respectively. Hereinafter the subscript $(\cdot)_h$ will denote the FE component and the tilde $\widetilde{(\cdot)}$ the subgrid component. Applying the two-scale

decomposition to (7) we obtain a discrete problem

$$(\partial_t \mathbf{u}_h, \mathbf{v}_h) + (\partial_t \tilde{\mathbf{u}}, \mathbf{v}_h) + B(\mathbf{a}; [\mathbf{u}_h, p_h], [\mathbf{v}_h, q_h]) + \left(\tilde{\mathbf{u}}, \mathcal{L}^*_{\mathbf{a}}(\mathbf{v}_h, q_h)\right)_h - (\tilde{p}, \nabla \cdot \mathbf{v}_h) = \langle \mathbf{f}, \mathbf{v}_h \rangle \,, \tag{13}$$

where $(\cdot,\cdot)_h = \sum_{K\in\mathcal{T}_h}(\cdot,\cdot)_K$ is the sum of scalar products (6) over each element K of the partition $\mathcal{T}_h$, and

$$\mathcal{L}^*_{\mathbf{a}}(\mathbf{v}_h, q_h) := -\nu\nabla^2\mathbf{v}_h - \mathbf{a}\cdot\nabla\mathbf{v}_h - \nabla q_h \tag{14}$$

is the formal of the adjoint operator of the momentum equation. The term involving the adjoint operator comes from an elementwise integration by parts of the terms involving the subscales, in which the boundary terms $\left(\mathbf{v}_h, \nu\mathbf{n}\cdot\nabla\tilde{\mathbf{u}}\right)_{\partial h}$ and $\left(q_h, \mathbf{n}\cdot\tilde{\mathbf{u}}\right)_{\partial h}$ have been neglected (the subscript ∂h is used to denote the sum over all elements of the integral on the boundary of each element). It also involves the approximation $b(\mathbf{a}, \tilde{\mathbf{u}}, \mathbf{u}_h) \approx -(\tilde{\mathbf{u}}, \mathbf{a}\cdot\nabla\mathbf{v}_h)$ which implies neglecting $\left(\mathbf{v}_h, \mathbf{n}\cdot\mathbf{a}\tilde{\mathbf{u}}\right)_{\partial h}$ and $(\tilde{\mathbf{u}}, \nabla\cdot\mathbf{a}\mathbf{v}_h)$. These approximations are discussed in [22] together with the choice of $\mathbf{a}$ which defines the type of scale splitting (linear or nonlinear), also discussed below.

The discrete problem depends on $\tilde{\mathbf{u}} \in \widetilde{\mathcal{V}}_0$ and on $\tilde{p} \in \widetilde{\mathcal{Q}}_0$, $\widetilde{\mathcal{V}}_0$ and $\widetilde{\mathcal{Q}}_0$ being infinite-dimensional. Therefore, the equations for $\tilde{\mathbf{u}}$ and $\tilde{p}$ obtained after applying the two-scale decomposition cannot be directly solved, but some modeling steps are needed to obtain a feasible method. Considering the subscale as a time-dependent variable of the problem (see below) and approximating the Navier–Stokes operator by two stabilization parameters τ_m^{-1} and τ_c^{-1} (see for example [22]), the fine scale problem can be written as

$$\partial_t\tilde{\mathbf{u}} + \tau_m^{-1}\tilde{\mathbf{u}} = \mathcal{P}(\mathbf{R}_u), \tag{15}$$

$$\tau_c^{-1}\tilde{p} = \mathcal{P}(R_p). \tag{16}$$

In (15)–(16) $\mathcal{P}$ denotes the projection onto the space of subscales, which is discussed below. In turn, the vector $\mathbf{R}$ is the residual of the Navier–Stokes equations (1)–(2), defined as $\mathbf{R} = [\mathbf{R}_u, R_p]^T$, with

$$\mathbf{R}_u = \mathbf{f} - \partial_t\mathbf{u}_h - \mathcal{L}_{\mathbf{a}}(\mathbf{u}_h, p_h), \tag{17}$$

$$R_p = -\nabla\cdot\mathbf{u}_h \tag{18}$$

where

$$\mathcal{L}_{\mathbf{a}}(\mathbf{v}_h, q_h) := -\nu\nabla^2\mathbf{v}_h + \mathbf{a}\cdot\nabla\mathbf{v}_h + \nabla q_h. \tag{19}$$

Finally, the expression of the stabilization parameter τ_m is

$$\tau_m = \left(\frac{c_1\nu}{h^2} + \frac{c_2|\mathbf{a}|}{h}\right)^{-1}, \tag{20}$$

whereas we consider two possible definitions of τ_c, viz. $\tau_c = 0$ (which implies $\tilde{p} = 0$) and

$$\tau_c = \frac{h^2}{c_1\tau_m}, \tag{21}$$

where h is the mesh size and c_1 and c_2 are algorithmic constants. Let us comment on expression (20):

- The influence of the constants c_1 and c_2 is discussed in Section 8. A theoretical way to determine them would be to impose that the numerical dissipation they introduce be equal to the molecular dissipation in turbulent regimes, as explained in [42].
- The definition of τ_m in (20) is not standard, in the sense that the one used often depends on the time step size of the time discretization, δt. Instead of (20), $\tau_m^{-1} = \frac{1}{\delta t} + \frac{c_1\nu}{h^2} + \frac{c_2|\mathbf{a}|}{h}$ is more often considered (see, e.g., [24,39]). We refer to Section 9 for a more detailed discussion about this topic. Likewise, other expressions with the same asymptotic behavior in terms of h, ν and $|\mathbf{a}|$ can also be employed.
- Expression (20) corresponds to linear isotropic elements. If elements of order p are used (p is not the pressure, here), c_1 must be replaced by $c_1 p^4$ and c_2 by $c_2 p$. For anisotropic elements, the definition of h within each element is not obvious. A possibility is explained in [43].

In the following three sections we discuss the particular ingredients of our VMS models. A different summary can also be found in [44], together with some numerical experiments.

2.2.1. The dynamics of the subscales

Stabilized formulations were originally developed for steady convection–diffusion [10] and Stokes [8,9] problems. As the numerical instabilities have a spatial nature, the time dependency of the subscales was not considered, and the standard choice [11,12,18] was to take

$$\tilde{\mathbf{u}} = \tau_m \mathcal{P}(\mathbf{R}_u), \tag{22}$$

that is, to neglect the temporal derivative of the subscales in (15). In this case, the subscales are called quasi-static in what follows.

The subscale as a time dependent variable of the problem was introduced in [16,22]. It gives rise to important properties like commutativity of space and time discretization, stability without restrictions on the time step size [22,45] and, combined with orthogonal subscales, convergence towards weak solutions of the Navier–Stokes equations [25] and the possibility of predicting backscatter [7,44].

Eq. (15) can be analytically integrated to give

$$\tilde{\mathbf{u}}(t^*) = \tilde{\mathbf{u}}(0) + \mu^{-1}(t^*) \int_0^{t^*} \mu(t) \mathcal{P}\mathbf{R}_u \mathrm{d}t, \qquad \mu(s) = \exp \int_0^s \tau^{-1}(t) \mathrm{d}t, \tag{23}$$

where it is explicitly seen that the subscale is not only a function of the residual but also of the flow history. In practice this integration is performed numerically, as described below.

2.2.2. (Non)linear scale splitting

The original VMS formulation [5,6] was developed having linear problems in mind and its extension to the Navier–Stokes equations was implicitly based on a "linearization", fixing the advection velocity and applying the multiscale splitting to the rest of the terms. A nonlinear scale splitting was used in [11,12] together with an explicit resolution of the small scales in which a Smagorinsky damping was introduced. A nonlinear scale splitting with modeled subscales was used in [16,18] and in [22], where it was shown that it leads to global conservation of momentum. We therefore consider both options

$$\mathbf{a} = \mathbf{u}_h \quad \text{for linear subscales,} \tag{24}$$

$$\mathbf{a} = \mathbf{u}_h + \tilde{\mathbf{u}} \quad \text{for nonlinear subscales.} \tag{25}$$

Remark 2.1. When we use the nonlinear definition for the advection velocity, $\mathbf{a} = \mathbf{u}_h + \tilde{\mathbf{u}}$, the skew-symmetric term *type* 2 (11) in the FE equation (13) reads:

$$b(\mathbf{a}, \mathbf{u}_h, \mathbf{v}_h) = ((\mathbf{u}_h + \tilde{\mathbf{u}}) \cdot \nabla \mathbf{u}_h, \mathbf{v}_h) + \frac{1}{2}(\mathbf{u}_h \cdot \mathbf{v}_h, \nabla \cdot \mathbf{u}_h) + \frac{1}{2}(\mathbf{u}_h \cdot \mathbf{v}_h, \nabla \cdot \tilde{\mathbf{u}}). \tag{26}$$

The last term is not well-defined, since it includes derivatives of the discontinuous subscale $\tilde{\mathbf{u}}$. One possibility is to neglect it (as previously done with other similar terms when arriving to (13)), which implies

$$b(\mathbf{a}, \mathbf{u}_h, \mathbf{u}_h) = -\frac{1}{2}(|\mathbf{u}_h|^2, \nabla \cdot \tilde{\mathbf{u}}), \tag{27}$$

the same result obtained when the non conservative form is used. By contrast, the skew-symmetric term *type* 1 in the FE equation (13) reads

$$b(\mathbf{a}, \mathbf{u}_h, \mathbf{v}_h) = \frac{1}{2}((\mathbf{u}_h + \tilde{\mathbf{u}}) \cdot \nabla \mathbf{u}_h, \mathbf{v}_h) - \frac{1}{2}((\mathbf{u}_h + \tilde{\mathbf{u}}) \cdot \mathbf{u}_h, \nabla \cdot \mathbf{v}_h) \tag{28}$$

from where

$$b(\mathbf{a}, \mathbf{u}_h, \mathbf{u}_h) = 0. \tag{29}$$

In Section 5.2 we will see the influence of the two forms of the convective term on the results. It is worth noting that the same approximations have been introduced in all cases to implement $b(\mathbf{a}, \tilde{\mathbf{u}}, \mathbf{u}_h)$, but these approximations are taken into account in the (usual) energy estimates of Section 3.

Remark 2.2. At the continuous level, the different expressions of the convective term are also equivalent to the so called conservation form

$$b(\mathbf{u}, \mathbf{v}, \mathbf{w}) = -(\mathbf{u} \otimes \mathbf{v}, \nabla \mathbf{w}).$$

In the discrete problem, the nonlinear scale splitting leads to the following terms in the momentum equation:

$$b(\mathbf{a}, \mathbf{u}_h + \tilde{\mathbf{u}}, \mathbf{v}_h) = -(\mathbf{u}_h \otimes \mathbf{u}_h, \nabla \mathbf{v}_h) - (\mathbf{u}_h \otimes \tilde{\mathbf{u}}, \nabla \mathbf{v}_h) - (\tilde{\mathbf{u}} \otimes \mathbf{u}_h, \nabla \mathbf{v}_h) - (\tilde{\mathbf{u}} \otimes \tilde{\mathbf{u}}, \nabla \mathbf{v}_h). \tag{30}$$

Even if this is not exactly what we get using the non-conservative or skew-symmetric forms because of the approximation error, this allows us to interpret the different contributions arising from the nonlinear scale splitting. As it is explained in [44], from (30) we can identify the contributions from the cross stresses, the Reynolds stresses and the subgrid scale tensor.

2.2.3. The space for the subscales

The selection of the space for the approximation of the subscales determines the projection $\mathcal{P}$ appearing in the right-hand side of (15) and (16). The first option, already considered in [11,12,18] and named Algebraic Subgrid Scale (ASGS) in [21], is to take the subscales in the space of the residuals, that is,

$$\mathcal{P} := \mathbf{I}. \tag{31}$$

Another possibility introduced in [21] is to consider the space of the subscales orthogonal to the FE space. The main motivation of the method is that a stability estimate for the projection onto the FE space of the pressure and/or the convective terms can already be obtained in the standard Galerkin method and therefore the only "missing" part is the orthogonal one. The Orthogonal Subscales (OSS) method is then characterized by the following projection definition:

$$\mathcal{P} := \Pi_h^{\perp} = \mathbf{I} - \Pi_h, \tag{32}$$

where Π_h is the projection onto the FE space. With this choice, the residual of the momentum equation does not depend on $\partial_t \mathbf{u}_h$. Likewise, $\mathcal{P}(\mathbf{f})$ in this case is only well defined for $\mathbf{f} \in L^2(\Omega)^d$. In the case of minimum regularity, $\mathbf{f} \in H^{-1}(\Omega)^d$, this term can be simply neglected without upsetting the accuracy of the method.

In fact, with this choice, the orthogonality between the space of subscales and the FE space is only guaranteed when the stabilization parameters are constant. If this is not the case, the method is still optimally convergent [46] but this property is lost. In order to have truly orthogonal subscales, *which guarantees a proper separation of the FE and the subgrid scale kinetic energies* (see below and Section 3) a slight modification of the projection Π_h is needed (see [46]). We will use two different weighted projections: one for the velocity subscales (Π_m) in (15) and another for the pressure subscales (Π_c) in (16). We define the weighted projections Π_m and Π_c such that given any vector $\mathbf{w} \in \mathcal{V}_0$ and any scalar $r \in \mathcal{Q}_0$ we have

$$(\tau_m \Pi_m(\mathbf{w}), \mathbf{v}_h) = (\tau_m \mathbf{w}, \mathbf{v}_h) \quad \forall \mathbf{v}_h \in \mathcal{V}_{0,h}, \tag{33}$$

$$(\tau_c \Pi_c(r), q_h) = (\tau_c r, q_h) \quad \forall q_h \in \mathcal{Q}_{0,h}. \tag{34}$$

These definitions guarantee the orthogonality between the FE and subscale spaces in the case of static subscales, that is, neglecting temporal derivatives in (15). It then follows that the term containing the temporal derivative of the subscale in the FE equation (13) also vanishes.

However, if the dynamic version of the method is used, the weight of the projection (33) must be conveniently modified to ensure the mentioned orthogonality. As it can be seen in (23), the definition of the weight depends on the time integration strategy, as explicitly stated in Section 4.

3. Energy balance statements

In this section we revisit global energy conservation statements of the method. As shown in [7], similar statements can be obtained locally (in a volume $\omega \subset \Omega$).

Taking $\mathbf{v}_h = \mathbf{u}_h$ and $q_h = p_h$ in (13) we have the energy balance on the FE component

$$\underbrace{\frac{1}{2} d_t \|\mathbf{u}_h\|^2}_{\text{I}} + \underbrace{\nu \|\nabla \mathbf{u}_h\|^2}_{\text{II}} + \underbrace{b(\mathbf{a}, \mathbf{u}_h, \mathbf{u}_h)}_{\text{III}} + \underbrace{(\partial_t \tilde{\mathbf{u}}, \mathbf{u}_h) + \left(\tilde{\mathbf{u}}, \mathcal{L}^*_{\mathbf{a}}(\mathbf{u}_h, p_h)\right)_h - (\tilde{p}, \nabla \cdot \mathbf{u}_h)}_{\text{IV}} = \underbrace{\langle \mathbf{f}, \mathbf{u}_h \rangle}_{\text{V}}. \tag{35}$$

In Eq. (35) we group the terms as

(I)	FE kinetic energy variation:	$\frac{1}{2}d_t\|\mathbf{u}_h\|^2$
(II)	FE viscous dissipation:	$\nu\|\nabla\mathbf{u}_h\|^2$
(III)	FE convective term:	$b(\mathbf{a},\mathbf{u}_h,\mathbf{u}_h)$
(IV)	FE to SGS energy transfer:	$\varepsilon_h = (\partial_t\tilde{\mathbf{u}},\mathbf{u}_h)+\left(\tilde{\mathbf{u}},\mathcal{L}^*_{\mathbf{a}}(\mathbf{u}_h,p_h)\right)_h-(\tilde{p},\nabla\cdot\mathbf{u}_h)$
(V)	FE component of external power:	$\langle\mathbf{f},\mathbf{u}_h\rangle$

Multiplying (15) by $\tilde{\mathbf{u}}$ and (16) by $\tilde{p}$, integrating over the domain and decomposing the residual of the momentum equation as $\mathbf{R}_u = \mathbf{f}-\partial_t\mathbf{u}_h-\mathcal{L}_{\mathbf{a}}(\mathbf{u}_h,p_h)$, we obtain the global energy balance on the fine scale

$$\underbrace{\frac{1}{2}d_t\|\tilde{\mathbf{u}}\|^2}_{\text{I}}+\underbrace{\tau_m^{-1}\|\tilde{\mathbf{u}}\|^2}_{\text{II}}+\underbrace{\tau_c^{-1}\|\tilde{p}\|^2}_{\text{III}}$$
$$+\underbrace{\left(\mathcal{P}(\partial_t\mathbf{u}_h),\tilde{\mathbf{u}}\right)+\left(\mathcal{P}(\mathcal{L}_{\mathbf{a}}(\mathbf{u}_h,p_h)),\tilde{\mathbf{u}}\right)_h+(\mathcal{P}(\nabla\cdot\mathbf{u}_h),\tilde{p})}_{\text{IV}}=\underbrace{\left(\mathcal{P}(\mathbf{f}),\tilde{\mathbf{u}}\right)}_{\text{V}}. \tag{36}$$

We group the terms in (36) as

(I)	SGS kinetic energy variation:	$\frac{1}{2}d_t\|\tilde{\mathbf{u}}\|^2$
(II)	SGS velocity dissipation:	$\tau_m^{-1}\|\tilde{\mathbf{u}}\|^2$
(III)	SGS pressure dissipation:	$\tau_c^{-1}\|\tilde{p}\|^2$
(IV)	SGS to FE energy transfer:	$\tilde{\varepsilon} = \left(\mathcal{P}(\partial_t\mathbf{u}_h),\tilde{\mathbf{u}}\right)+\left(\tilde{\mathbf{u}},\mathcal{P}(\mathcal{L}_{\mathbf{a}}(\mathbf{u}_h,p_h))\right)_h+(\tilde{p},\mathcal{P}(\nabla\cdot\mathbf{u}_h))$
(V)	SGS component of external power:	$\left(\mathcal{P}(\mathbf{f}),\tilde{\mathbf{u}}\right)$

Finally, adding up Eqs. (35) and (36) we obtain an equation for the total kinetic energy

$$\begin{aligned}&\frac{1}{2}d_t\|\mathbf{u}_h\|^2+\frac{1}{2}d_t\|\tilde{\mathbf{u}}\|^2+\nu\|\nabla\mathbf{u}_h\|^2+b(\mathbf{a},\mathbf{u}_h,\mathbf{u}_h)+\tau_m^{-1}\|\tilde{\mathbf{u}}\|^2+\tau_c^{-1}\|\tilde{p}\|^2\\&\quad+(\partial_t\tilde{\mathbf{u}},\mathbf{u}_h)+\left(\mathcal{P}(\partial_t\mathbf{u}_h),\tilde{\mathbf{u}}\right)+\left(\mathcal{P}(\mathcal{L}_{\mathbf{a}}(\mathbf{u}_h,p_h))+\mathcal{L}^*_{\mathbf{a}}(\mathbf{u}_h,p_h),\tilde{\mathbf{u}}\right)_h\\&\quad+(\mathcal{P}(\nabla\cdot\mathbf{u}_h)-\nabla\cdot\mathbf{u}_h,\tilde{p})=\langle\mathbf{f},\mathbf{u}_h\rangle+\left(\mathcal{P}(\mathbf{f}),\tilde{\mathbf{u}}\right).\end{aligned} \tag{37}$$

Let us note the presence of $b(\mathbf{a},\mathbf{u}_h,\mathbf{u}_h)$, which is zero only when the skew-symmetric type 1 form is considered. Other choices could result in a spurious positive contribution to the FE kinetic energy as it is actually observed in the DHIT problem, and could result in a loss of stability, although that was not observed.

3.1. Static subscales

In this case the energy balance for the subscale is meaningless because there are explicit expressions for the subscales (22) and (16). When (22) and (16) are used in (35), we obtain

$$\begin{aligned}&\frac{1}{2}d_t\|\mathbf{u}_h\|^2+\nu\|\nabla\mathbf{u}_h\|^2+b(\mathbf{a},\mathbf{u}_h,\mathbf{u}_h)+\left(\tau_m\mathcal{P}\left(\partial_t\mathbf{u}_h\right),\mathcal{L}^*_{\mathbf{a}}(\mathbf{u}_h,p_h)\right)_h\\&\quad+\left(\tau_m\mathcal{P}\left(\mathcal{L}_{\mathbf{a}}(\mathbf{u}_h,p_h)\right),\mathcal{L}^*_{\mathbf{a}}(\mathbf{u}_h,p_h)\right)_h+\tau_c\left\|\mathcal{P}(\nabla\cdot\mathbf{u}_h)\right\|^2\\&=\langle\mathbf{f},\mathbf{u}_h\rangle+\left(\tau_m\mathcal{P}(\mathbf{f}),\mathcal{L}^*_{\mathbf{a}}(\mathbf{u}_h,p_h)\right)_h.\end{aligned} \tag{38}$$

In the case of the ASGS method, where $\mathcal{P}:=\mathbf{I}$, the fourth term on the left hand side is a source of problems. On the one hand, it cannot be neglected because it is needed to make the method consistent. On the other hand, it can only be controlled by the dissipation of the time integration scheme and is therefore responsible for the introduction of a restriction on the time step size. As a side problem, it is very inconvenient for an implementation if any explicit (operator splitting) time integration is chosen as it results in a non-symmetric mass matrix. This term is not present if the OSS method is chosen using the projection $\mathcal{P}:=\mathbf{I}-\Pi_h$. Stability of both the fully discrete and the semidiscrete Stokes problem has been proven in [45].

The important term is the fifth one, which permits to control $\tau_m \|\mathcal{P}(\mathbf{a}\cdot\nabla\mathbf{u}_h + \nabla p_h)\|^2$; the FE part in the OSS formulation is readily controlled using inverse estimates. It therefore provides the essential numerical stability. The last term acts as a penalty on the divergence constraint, adding volumetric diffusion and provides (extra, non-essential) numerical stability.

For the OSS method, it is proved in [42] that the dissipative structure of the discrete problem has the same statistical behavior in fully developed turbulence than the continuous problem, in the sense that this dissipation has the same estimates as the molecular one. Both dissipations could be made equal by a proper choice of the stabilization parameters in (20). This, however, requires a small change in the advection velocity of this expression, which depends on an integral length of the problem. See [42] for details.

3.2. Dynamic subscales

In this case, the time derivative of both the FE and subgrid components has to be considered and an estimator for the kinetic energy variation of both the FE and subgrid velocity can be obtained. The stability of the subgrid scale velocity can then be used to obtain a stability estimate of the FE component in a norm that includes the convective and pressure terms [22,45,47].[2] Therefore, the numerical dissipation of the method is actually given by the energy transfer ε_h from the FE to the subscale component. Using (15)–(16), we get:

$$\begin{aligned}\varepsilon_h = &\left(\partial_t\tilde{\mathbf{u}}, \mathbf{u}_h\right) - \left(\tau_m\partial_t\tilde{\mathbf{u}}, \mathcal{L}^*_{\mathbf{a}}(\mathbf{u}_h, p_h)\right)_h - \left(\tau_m\mathcal{P}\left(\partial_t\mathbf{u}_h\right), \mathcal{L}^*_{\mathbf{a}}(\mathbf{u}_h, p_h)\right)_h \\ &- \left(\tau_m\mathcal{P}\left(\mathcal{L}_{\mathbf{a}}(\mathbf{u}_h, p_h)\right), \mathcal{L}^*_{\mathbf{a}}(\mathbf{u}_h, p_h)\right)_h + \tau_c\left\|\mathcal{P}\nabla\cdot\mathbf{u}_h\right\|^2. \end{aligned} \tag{39}$$

Except from the viscous contribution, the last two terms in (39) are positive, providing dissipation of the FE energy, but the first three could be negative, providing these models with a mechanism to predict a backward energy transfer, not frequently found in classical LES models [1]. It is justified in [44] that even if the first three terms may be negative at a certain time instant, their averaged contribution in a time window greater than the largest period needs to be positive, which is the behavior expected of backscatter from a physical point of view.

For the ASGS method, i.e., $\mathcal{P} := \mathbf{I}$, the last term on the left hand side of (37) vanishes and the previous one reads

$$\left(\mathcal{L}_{\mathbf{a}}(\mathbf{u}_h, p_h) + \mathcal{L}^*_{\mathbf{a}}(\mathbf{u}_h, p_h), \tilde{\mathbf{u}}\right)_h = -2\left(\nu\Delta\mathbf{u}_h, \tilde{\mathbf{u}}\right)_h. \tag{40}$$

In turn, the time derivatives of the FE and subscale velocities can be combined as

$$\frac{1}{2}d_t\|\mathbf{u}_h\|^2 + \frac{1}{2}d_t\|\tilde{\mathbf{u}}\|^2 + \left(\partial_t\tilde{\mathbf{u}}, \mathbf{u}_h\right) + \left(\partial_t\mathbf{u}_h, \tilde{\mathbf{u}}\right) = \frac{1}{2}d_t\|\mathbf{u}_h + \tilde{\mathbf{u}}\|^2 \tag{41}$$

to rewrite (37) as

$$\frac{1}{2}d_t\|\mathbf{u}_h + \tilde{\mathbf{u}}\|^2 + \nu\|\nabla\mathbf{u}_h\|^2 + b(\mathbf{a}, \mathbf{u}_h, \mathbf{u}_h) + \tau_m^{-1}\|\tilde{\mathbf{u}}\|^2 + \tau_c^{-1}\|\tilde{p}\|^2 - 2\left(\nu\Delta\mathbf{u}_h, \tilde{\mathbf{u}}\right) = \langle\mathbf{f}, \mathbf{u}_h\rangle + \left\langle\mathbf{f}, \tilde{\mathbf{u}}\right\rangle. \tag{42}$$

From this equation, a stability estimate for $\|\mathbf{u}_h + \tilde{\mathbf{u}}\|$ can be obtained as the last term on the left hand side can be controlled using the second one (see [45, Remark 4.7]).

Another important point of (42) is that it immediately shows that when the mesh is fine enough, i.e.,

$$\frac{|\mathbf{a}|\,h}{\nu} \ll 1,$$

the dissipation of the total energy depends only on the viscosity. Therefore, the dissipative structure is correctly predicted when a laminar flow is considered or when the discretization is fine enough to resolve all scales of the flow, an important advantage over other LES techniques.

On the other hand, for the OSS method, the FE and subgrid kinetic energy can be summed to obtain the total one

$$\frac{1}{2}d_t\|\mathbf{u}_h\|^2 + \frac{1}{2}d_t\|\tilde{\mathbf{u}}\|^2 = \frac{1}{2}d_t\|\mathbf{u}_h + \tilde{\mathbf{u}}\|^2 \tag{43}$$

[2] However, it should be kept in mind that the numerical solution of the problem is the FE component. There is no reason to add the subscale to the final solution as the approximation is limited by the interpolation order, see [22, Remark 10].

since $(\partial_t \tilde{\mathbf{u}}, \mathbf{u}_h) = (\partial_t \mathbf{u}_h, \tilde{\mathbf{u}}) = 0$ as soon as we enforce the subscale to be orthogonal to the FE space. This property also guarantees that

$$\left(\Pi_m(\mathcal{L}_{\mathbf{a}}(\mathbf{u}_h, p_h)), \tilde{\mathbf{u}}\right) = 0 \tag{44}$$

$$(\Pi_c(\nabla \cdot \mathbf{u}_h), \tilde{p}) = 0 \tag{45}$$

which implies that the last term on the left hand side of (37) vanishes and that the previous one can be written as

$$\left(\mathcal{P}(\mathcal{L}_{\mathbf{a}}(\mathbf{u}_h, p_h)) + \mathcal{L}^*_{\mathbf{a}}(\mathbf{u}_h, p_h), \tilde{\mathbf{u}}\right)_h = \left(\mathcal{L}_{\mathbf{a}}(\mathbf{u}_h, p_h) + \mathcal{L}^*_{\mathbf{a}}(\mathbf{u}_h, p_h), \tilde{\mathbf{u}}\right)_h = -2\left(\nu \Delta \mathbf{u}_h, \tilde{\mathbf{u}}\right)_h \tag{46}$$

as in the ASGS case. Let us note that the Laplacian term can be eliminated without affecting the convergence properties of the method. Then, the global energy balance equation (37) reads

$$\frac{1}{2} d_t \|\mathbf{u}_h\|^2 + \frac{1}{2} d_t \|\tilde{\mathbf{u}}\|^2 + \nu \|\nabla \mathbf{u}_h\|^2 + b(\mathbf{a}, \mathbf{u}_h, \mathbf{u}_h) + \tau_m^{-1} \|\tilde{\mathbf{u}}\|^2 + \tau_c^{-1} \|\tilde{p}\|^2 = \langle \mathbf{f}, \mathbf{u}_h \rangle + \left(\mathcal{P}(\mathbf{f}), \tilde{\mathbf{u}}\right), \tag{47}$$

which is exactly (42) except for the projection of the force in the last term. Stability and convergence of this formulation have been proved in [25,47].

4. Final discrete problem

Applying a time integration algorithm to (13)–(15)–(16) we get the fully discrete problem. The final implementation of the discrete problem is written here considering a Picard linearization of the convective term and the Backward Euler (BE) scheme for the time discretization. It can be straightforwardly modified to consider the Crank–Nicolson time integration scheme; this last scheme is the one used in the numerical examples of Sections 5–7.

4.1. Algebraic Subgrid Scales (ASGS)

Taking the nonlinear advection velocity definition (25) and considering the time derivative in the fine scales, we have the Dynamic and Nonlinear ASGS method, hereinafter Dyn-Nl-ASGS. At time step n and nonlinear iteration i, given $\mathbf{u}_h^{n,i-1}$, $\mathbf{u}_h^{n-1}$, $\tilde{\mathbf{u}}^{n,i-1}$ and $\tilde{\mathbf{u}}^{n-1}$ we compute $\mathbf{u}_h^{n,i}$ and $p_h^{n,i}$ such that

$$\begin{aligned}
&\frac{1}{\delta t}(\mathbf{u}_h^{n,i}, \mathbf{v}_h) + B(\mathbf{a}^{n,i-1}; [\mathbf{u}_h^{n,i}, p_h^{n,i}], [\mathbf{v}_h, q_h]) + \left(\tau_{m,t}\left[\frac{1}{\delta t}\mathbf{u}_h^{n,i} + \mathcal{L}_{\mathbf{a}^{n,i-1}}(\mathbf{u}_h^{n,i}, p_h^{n,i})\right], \mathcal{L}^*_{\mathbf{a}^{n,i-1}}(\mathbf{v}_h, q_h)\right)_h \\
&\quad + \left(\tau_c \nabla \cdot \mathbf{u}_h^{n,i}, \nabla \cdot \mathbf{v}_h\right) - \frac{1}{\delta t}\left(\tau_{m,t}\left[\frac{1}{\delta t}\mathbf{u}_h^{n,i} + \mathcal{L}_{\mathbf{a}^{n,i-1}}(\mathbf{u}_h^{n,i}, p_h^{n,i})\right], \mathbf{v}_h\right)_h \\
&= \langle \mathbf{v}_h, \mathbf{f} \rangle + \frac{1}{\delta t}(\mathbf{u}_h^{n-1}, \mathbf{v}_h) + \frac{1}{\delta t}(\tilde{\mathbf{u}}^{n-1}, \mathbf{v}_h) - \frac{1}{\delta t}\left(\tau_{m,t}\left[\frac{1}{\delta t}\mathbf{u}_h^{n-1} + \mathbf{f} + \frac{1}{\delta t}\tilde{\mathbf{u}}^{n-1}\right], \mathbf{v}_h\right) \\
&\quad + \left(\tau_{m,t}\left[\frac{1}{\delta t}\mathbf{u}_h^{n-1} + \mathbf{f} + \frac{1}{\delta t}\tilde{\mathbf{u}}^{n-1}\right], \mathcal{L}^*_{\mathbf{a}^{n,i-1}}(\mathbf{v}_h, q_h)\right)_h,
\end{aligned} \tag{48}$$

where $\tau_{m,t} = \left(\delta t^{-1} + \tau_m^{-1}\right)^{-1}$ and $\mathbf{a}^{n,i-1} = \mathbf{u}_h^{n,i-1} + \tilde{\mathbf{u}}^{n,i-1}$.

In turn, $\tilde{\mathbf{u}}^{n,i}$ is computed by solving the discretization of the fine scale problem (15). Note that in the nonlinear version of the algorithm, the stabilization parameter $\tau_{m,t}$ depends on the subscale itself through $\mathbf{a}$ in (20), making the fine scale equation also nonlinear, although it is local and does not increase the size of the global linear system to be solved. At each integration point of each element we iteratively solve

$$\tilde{\mathbf{u}}^{n,i,k} = \tau_{m,t}^{k-1}\frac{1}{\delta t}\tilde{\mathbf{u}}^{n-1} + \tau_{m,t}^{k-1}\left[\mathbf{f} - \frac{(\mathbf{u}_h^{n,i} - \mathbf{u}_h^{n-1})}{\delta t} - \mathcal{L}_{\mathbf{a}^{n,i,k-1}}(\mathbf{u}_h^{n,i}, p_h^{n,i})\right] \tag{49}$$

where $\mathbf{a}^{n,i,k-1} = \mathbf{u}_h^{n,i} + \tilde{\mathbf{u}}^{n,i,k-1}$ is used in (20) to obtain $\tau_{m,t}^{k-1}$.

Alternatively, one can send the corresponding fine scale convective term $\tilde{\mathbf{u}} \cdot \nabla \mathbf{u}_h$ to the left-hand side, improving the convergence of the iterative process as

$$\tilde{\mathbf{u}}^{n,i,k} + \tilde{\mathbf{u}}^{n,i,k} \cdot \nabla \mathbf{u}_h^{n,i} = \tau_{m,t}^{k-1} \frac{1}{\delta t} \tilde{\mathbf{u}}^{n-1} + \tau_{m,t}^{k-1} \left[\mathbf{f} - \frac{(\mathbf{u}_h^{n,i} - \mathbf{u}_h^{n-1})}{\delta t} - \mathcal{L}_{\mathbf{u}_h^{n,i}}(\mathbf{u}_h^{n,i}, p_h^{n,i}) \right]. \tag{50}$$

This is a simple fixed-point iterative scheme that we have found efficient and robust for the numerical simulations presented in this paper, although in other situations we have found more convenient to use a conventional Newton–Raphson scheme to solve the nonlinear subscale equation [23].

For the simplest ASGS scheme we do not consider the time derivative of the fine scale, we consider them quasi-static, i.e., $(\partial_t \tilde{\mathbf{u}}, \mathbf{v}_h) = 0$. Note that in any case the subscales will depend on time through the FE residual and the stabilization parameter. On the other hand, the advection velocity is considered to be linear as indicated in (24). We label this method as Static Linear ASGS (Sta-Lin-ASGS). Note that the Sta-Lin-ASGS method does not need to explicitly compute $\tilde{\mathbf{u}}$; invoking (20) and (21) in (13) we get a discrete equation only in terms of the FE component.

We can readily define the rest of possible combinations of time and nonlinear treatment considering the linear advection velocity definition and the time-dependence in the subscales (Dyn-Lin-ASGS method) or keeping the static definition of the subscales with the nonlinear choice for the advection velocity (Sta-Nl-ASGS method).

4.2. Orthogonal Subscales (OSS)

Let us state the Dynamic and Nonlinear OSS (Dyn-Nl-OSS) method, which means to take into account the nonlinearity of the advection velocity (25) and the time derivative of the subscales. At time step n and nonlinear iteration i, given $\mathbf{u}_h^{n,i-1}$, $\mathbf{u}_h^{n-1}$, $\tilde{\mathbf{u}}^{n,i-1}$ and $\tilde{\mathbf{u}}^{n-1}$ we compute $\mathbf{u}_h^{n,i}$ and $p_h^{n,i}$ by solving

$$\begin{aligned}
&\frac{1}{\delta t}(\mathbf{u}_h^{n,i}, \mathbf{v}_h) + B(\mathbf{a}^{n,i-1}; [\mathbf{u}_h^{n,i}, p_h^{n,i}], [\mathbf{v}_h, q_h]) \\
&\quad + \left(\tau_{m,t} \left[\frac{1}{\delta t} \mathbf{u}_h^{n,i} + \mathcal{L}_{\mathbf{a}^{n,i-1}}(\mathbf{u}_h^{n,i}, p_h^{n,i}) \right], \mathcal{L}^*_{\mathbf{a}^{n,i-1}}(\mathbf{v}_h, q_h) \right) + \left(\tau_c \nabla \cdot \mathbf{u}_h^{n,i}, \nabla \cdot \mathbf{v}_h \right) \\
&= \langle \mathbf{v}_h, \mathbf{f} \rangle + \frac{1}{\delta t}(\mathbf{u}_h^{n-1}, \mathbf{v}_h) + \left(\tau_{m,t} \left[\mathbf{f} + \frac{1}{\delta t} \tilde{\mathbf{u}}^{n-1} - \boldsymbol{\xi}_m^{n,i-1} \right], \mathcal{L}^*_{\mathbf{a}^{n,i-1}}(\mathbf{v}_h, q_h) \right) - \left(\tau_c \xi_c^{n,i-1}, \nabla \cdot \mathbf{v}_h \right),
\end{aligned} \tag{51}$$

where $\boldsymbol{\xi}_m$ and ξ_c are the weighted projections of the residuals $\mathbf{R}_u$ and R_p (see below) evaluated at the corresponding time step and nonlinear iteration.

Like the Dyn-NL-ASGS method, we also need to compute the subscale velocity $\tilde{\mathbf{u}}$ explicitly. We compute the discrete subscale problem with the OSS counterpart of (49) or (50), viz.

$$\tilde{\mathbf{u}}^{n,i,k} + \tilde{\mathbf{u}}^{n,i,k} \cdot \nabla \mathbf{u}_h^{n,i} = \tau_{m,t}^{k-1} \frac{1}{\delta t} \tilde{\mathbf{u}}^{n-1} + \tau_{m,t}^{k-1} \left[\mathbf{f} - \frac{(\mathbf{u}_h^{n,i} - \mathbf{u}_h^{n-1})}{\delta t} - \mathcal{L}_{\mathbf{u}_h^{n,i}}(\mathbf{u}_h^{n,i}, p_h^{n,i}) \right] - \tau_{m,t}^{k-1} \boldsymbol{\xi}_m^{n,i-1}. \tag{52}$$

Note that $\boldsymbol{\xi}_m^{n,i}$ actually depends on $\tilde{\mathbf{u}}^{n,i}$ via the advection velocity of the convective term $\mathbf{a}^{n,i} = \mathbf{u}_h^{n,i} + \tilde{\mathbf{u}}^{n,i}$. In order to simplify the fine scale computation (52) we use the projection at the previous nonlinear iteration, i.e., $\boldsymbol{\xi}_m^{n,i-1}$.

For the dynamic OSS case we should introduce some modifications in the computation of the projection Π_m. At the fully discrete level, in order for $\tilde{\mathbf{u}}^{n+1}$ to be L^2 orthogonal to $\mathcal{V}_h$, we must add to the FE residual the subscale time derivative contribution from the previous time step and use $\tau_{m,t}$ instead of τ_m in the computation of the projections. Finally, the projections of the residuals onto the FE spaces $\boldsymbol{\xi}_m^{n,i}$ and $\xi_c^{n,i}$ are such that

$$(\tau_{m,t} \boldsymbol{\xi}_m^{n,i}, \mathbf{v}_h) = \left(\tau_{m,t} \left(\mathbf{R}_u^{n,i} + \frac{1}{\delta t} \tilde{\mathbf{u}}^{n-1} \right), \mathbf{v}_h \right) \quad \forall \mathbf{v}_h \in \mathcal{V}_{0,h}, \tag{53}$$

$$(\tau_c \xi_c^{n,i}, q_h) = (\tau_c R_p^{n,i}, q_h) \quad \forall q_h \in \mathcal{Q}_{0,h}, \tag{54}$$

where the residuals $\mathbf{R}_u^{n,i}$ and $R_p^{n,i}$ are evaluated using (17) and (18) with $\mathbf{a}^{n,i} = \mathbf{u}_h^{n,i} + \tilde{\mathbf{u}}^{n,i}$, $\mathbf{u}_h^{n,i}$, $\mathbf{u}_h^{n-1}$ and $p_h^{n,i}$. Note that when convergence of the nonlinear iteration is achieved, (52) and (53) guarantee that $(\mathbf{v}_h, \tilde{\mathbf{u}}^n) = 0$ for any $\mathbf{v}_h \in \mathcal{V}_{0,h}$.

Table 1
DHIT test cases.

Case id.	Label	Method	Advection velocity ($\mathbf{a}$)	Subscales tracking
1	Sta-Lin-ASGS	ASGS	Linear ($\mathbf{a} = \mathbf{u}_h$)	Static ($\partial_t \tilde{\mathbf{u}} = \mathbf{0}$)
2	Dyn-Lin-ASGS	ASGS	Linear ($\mathbf{a} = \mathbf{u}_h$)	Dynamic ($\partial_t \tilde{\mathbf{u}} \neq \mathbf{0}$)
3	Dyn-Nl-ASGS	ASGS	Nonlinear ($\mathbf{a} = \mathbf{u}_h + \tilde{\mathbf{u}}$)	Dynamic ($\partial_t \tilde{\mathbf{u}} \neq \mathbf{0}$)
4	Sta-Lin-OSS	OSS	Linear ($\mathbf{a} = \mathbf{u}_h$)	Static ($\partial_t \tilde{\mathbf{u}} = \mathbf{0}$)
5	Dyn-Lin-OSS	OSS	Linear ($\mathbf{a} = \mathbf{u}_h$)	Dynamic ($\partial_t \tilde{\mathbf{u}} \neq \mathbf{0}$)
6	Dyn-Nl-OSS	OSS	Nonlinear ($\mathbf{a} = \mathbf{u}_h + \tilde{\mathbf{u}}$)	Dynamic ($\partial_t \tilde{\mathbf{u}} \neq \mathbf{0}$)

5. Decay of homogeneous isotropic turbulence

5.1. Problem definition

This problem, one of the most used benchmarks to test LES models, consists of analyzing the statistics of the turbulent flow in a 3D box of size $\Omega = (0, 2\pi) \times (0, 2\pi) \times (0, 2\pi)$ with periodic boundary conditions in all directions, which is started with a field having a predetermined energy spectrum. A detailed description of the computational domain, initial conditions, and problem setting is given in [48], which we follow here. A description on the influence of the domain size on the results is given in [49]. We solve this problem using the different VMS models of Section 4 and structured meshes with $N_x \times N_y \times N_z$ linear, quadratic and cubic hexahedral elements, taking $(N_x, N_y, N_z) = (32, 32, 32)$, $(64, 64, 64)$ and $(128, 128, 128)$.

5.1.1. Initial condition

The initial energy spectra [48] is given by

$$E(k, 0) = \frac{q^2}{2A} k_0^{-(\sigma+1)} k^4 \exp\left(-\frac{\sigma}{2}\left(\frac{k}{k_0}\right)^2\right), \tag{55}$$

where k_0 is the wave number at which $E(k, 0)$ is maximum, $q^2/2 = 3/2$ is the total kinetic energy, $\sigma = 4$ and $A = \int_0^\infty k^\sigma \exp(-\sigma k^2/2) = \frac{3}{32}\sqrt{\frac{\pi}{2}}$. Following Rogallo [50], we generate the initial field on the Fourier space such that it satisfies continuity and has the energy spectrum prescribed in (55). We finally transform the initial field to the physical space applying the inverse Fast Fourier Transform. We compare the results against those available in [51], so we set $k_0 = 6$ and the viscosity such that the associated Taylor-microscale Reynolds number is $\mathrm{Re}_\lambda = 952$, which results in $\nu = 3.5014006 \cdot 10^{-4}$.

5.1.2. Setting

We test the ASGS method and the OSS method reported in Section 4. The problem is solved considering three different cases for both methods, depending on the definition of the advection velocity and the tracking of the subscales. The advection velocity $\mathbf{a}$ can be linear or nonlinear and the subscales can be dynamic or static (see Section 2.2). Table 1 collects all the VMS combinations to be compared for the different simulations.

In terms of the numerical parameters of the methods, we use the skew-symmetric convective term *type* 1 defined in Section 2.1. The stabilization parameter τ_c is set equal to zero and the algorithmic constants in τ_m are $c_1 = 12$ and $c_2 = 2$ (see Section 8). Further, we use linear, quadratic, and cubic FEs.

The time integration has been performed using the Crank–Nicolson scheme with an adaptive time step. The initial time step is set to $\delta t_0 = 5.0 \cdot 10^{-3}$ and it is increased at each step multiplying it by an amplification factor. For this test the amplification is equal to 1.1, reading $\delta t_i = 1.1 \cdot \delta t_{i-1}$. The time step is increased step by step until it reaches a predefined threshold, e.g., 0.1 s. If convergence is not attained at either the nonlinear or solver loops, we apply a reduction factor (5.0 for this test) and recalculate the solution using the reduced time step, i.e., $\delta t_i = \frac{1}{5.0}\delta t_{i-1}$. The amplification of the time step when the solution converges allows one to decrease the total amount of time steps needed for the computation. At each time step the nonlinear system is solved as described in Section 4.

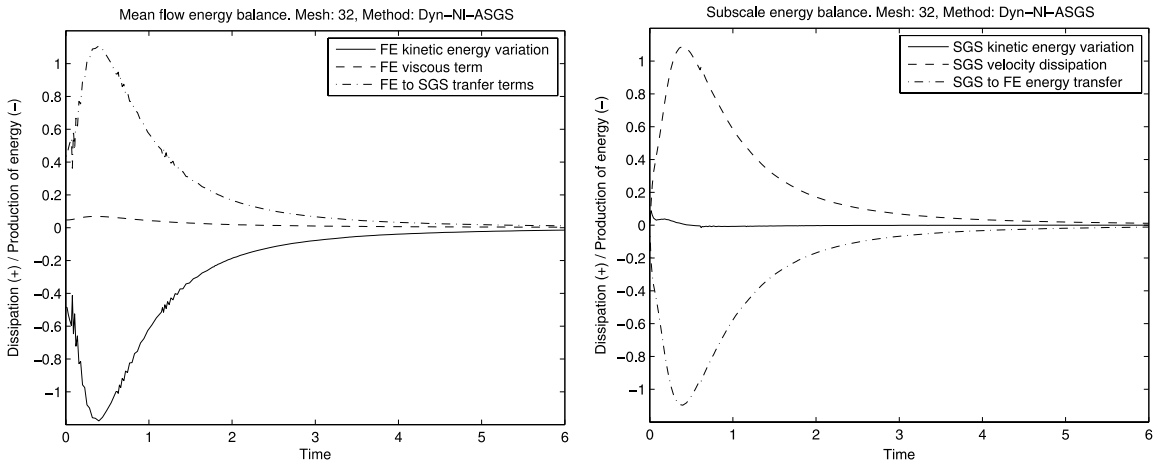

(a) Mean flow equation energy balance.

(b) Subscale equation energy balance.

Fig. 1. Mean flow and subscale energy balances for the Dyn-Nl-ASGS method.

5.2. Numerical results

5.2.1. Energy conservation

In this section we present results of the energy budget described in Section 3 obtained in a 32^3 elements mesh for the ASGS and OSS methods using the dynamic and nonlinear cases. Fig. 1 depicts the energy balance evolution for the mean flow equation (35) and the subscale equation (36) separately for the Dyn-Nl-ASGS case. It can be seen that the variation of kinetic energy shown by the FE component in Fig. 1(a) is offset in a large part by the transfer of energy to the subscales, while remaining energy on the mean flow balance is offset by the viscous term. On the other side, Fig. 1(b) shows that the energy transferred from the FE equation is mainly dissipated by the subscale velocity term. There is a small variation of the kinetic energy of the subscale at the beginning of the simulation. Note that since the viscosity is small, so are the viscous effects compared to the dissipation introduced by the subscale velocity. As we use a skew-symmetric form of the convective term, this term does not affect the energy balance and is not plotted in Fig. 1(a). Since $\tau_c = 0$, the pressure subscale term $\tau_c^{-1}\|\tilde{p}\|^2 = \tau_c\|\mathcal{P}(\nabla\cdot\mathbf{u}_h)\|^2$ is also zero and does not appear in Fig. 1(b).

The energy balance evolution for the mean flow and the subscales equations in (35)–(36) for the Dyn-Nl-OSS case are shown in Fig. 2. Fig. 2(a) depicts the energy balance evolution for the mean flow equation. Like for the ASGS method, the loss of kinetic energy is balanced by the FE scales to subscales energy transfer terms. The FE viscous term also has a very little impact on the dissipation of energy. On the other side, the subscales energy balance shown in Fig. 2(b) shows that almost all the energy transferred by the FE to the subscales is offset by the subscale velocity term, again like in the ASGS method. The only important difference between both methods is that *no oscillations are observed in the FE kinetic energy evolution when the OSS method is used.*

The global energy balance terms obtained solving the problem with the skew-symmetric convective term *type* 2 for the Dyn-Nl-ASGS and Dyn-Nl-OSS cases are shown in Fig. 3. We note that the loss of skew-symmetry in the convective term has a non-negligible effect (see Fig. 3(a) and (b)). In particular, this term introduces negative dissipation (production of energy) into the problem. This fact implies that the method is less dissipative and the energy decays at a slower rate than using the convective term *type* 1 and the method seems to be less diffusive. This negative contribution, however, is not predictable and could result in a blow up of the calculation. We refer to Section 8 for further comments about numerical instabilities associated to the *type* 2 convective term.

5.2.2. Computational cost analysis

The actual implementation in the parallel FE multiphysics code FEMPAR [52] is based on a classical domain decomposition strategy. At each nonlinear iteration the monolithic linear system is solved using a classical GMRES method applied to the Schur complement over the interfaces of the subdomains. This iterative procedure is preconditioned using a balancing Neumann–Neumann method applied to the monolithic system. The cost of each

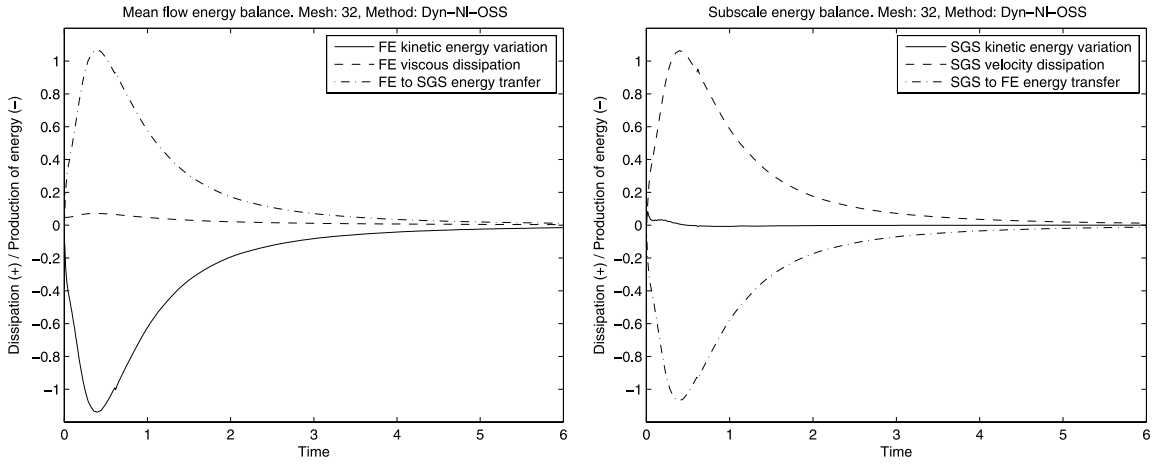

(a) Mean flow equation energy balance.

(b) Subscale equation energy balance.

Fig. 2. Mean flow and subscale energy balances for the Dyn-Nl-OSS method.

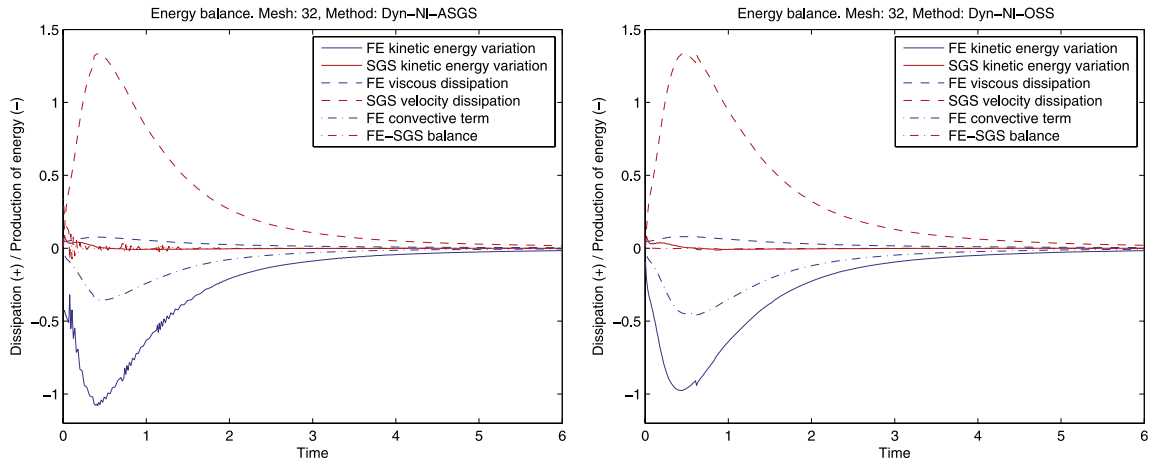

(a) Global energy balance for Dyn-Nl-ASGS.

(b) Global energy balance for Dyn-Nl-OSS.

Fig. 3. Global energy balance using skew-symmetric convective term *type 2*.

iteration is that of local Dirichlet solves for the Schur complement application and a local Neumann solve and a global solve for the preconditioner application (see [53–55]). All local systems are solved using the sparse direct solvers in PARDISO library [56,57].

An important issue when comparing different computational methods is their corresponding computational cost. In order to characterize the performance of the different VMS methods introduced in Section 2, we analyze some quantities that define the computational cost of each method, viz. nonlinear iterations, iterative solver iterations, and the adaptive time step evolution.

The cases compared here have been solved using 32^3 and 64^3 linear hexahedral element meshes. The 32^3 discretization is very coarse but it allows us to stress the differences between the proposed methods. In fact, due to this discretization, the linear and static ASGS case (Sta-Lin-ASGS) and the dynamic and linear ASGS case (Dyn-Lin-ASGS) do not converge at $t = 0.0$ and $t = 0.123$, respectively; the nonlinear iterations diverge even reducing the time step size. Anyway, all the methods converge as $h \to 0$.

The number of nonlinear iterations needed at each time step by the ASGS method is smaller than the one required by the OSS method in all cases. This is due to the evaluation of the projections at the previous nonlinear iteration $i - 1$; the implicit treatment of the projection is carried out by the nonlinear loop. Alternatively, since the projection is

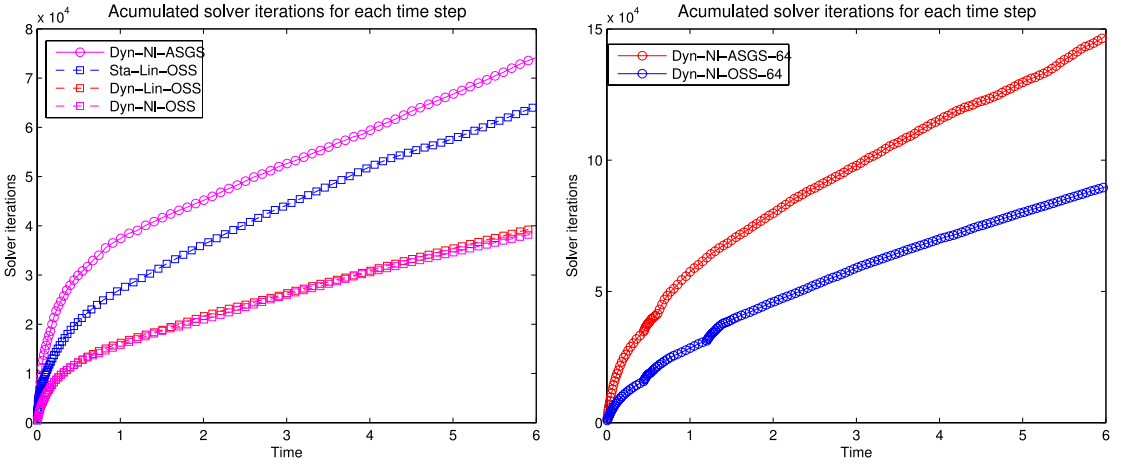

(a) 32^3 mesh. (b) 64^3 mesh.

Fig. 4. Accumulated solver iterations.

a linear operation, it can be performed together with the linear system [46], although a more involved implementation is required. Referring to the OSS method, we observe that the dynamic cases, both linear and nonlinear, need less iterations to achieve convergence without any significant difference between each other.

However, the number of nonlinear iterations is not the most relevant measure of the computational cost as the cost of each iteration is not fixed when iterative linear solvers are considered. Fig. 4 shows the accumulated number of solver iterations for each time step for the methods that have attained convergence with the 32^3 mesh (Fig. 4(a)) and for the dynamic versions with the 64^3 mesh (Fig. 4(b)). Unlike the nonlinear iterations, here we see that the ASGS method requires more solver iterations than OSS. The maximum solver iterations at each time step for the dynamic and nonlinear ASGS case is variable, starting from near 600, dropping to 200 and rising to around 300 iterations at the end of the computation. Meanwhile, all cases of the OSS method remain almost constant, around 60 iterations in the dynamic cases and around 40 iterations in the static one. The relation between time step size and solver iterations for each method is analyzed in Section 9.

The adaptive time stepping described in the previous subsection has an important role on the computational cost, as mentioned earlier. If the time step is reduced in order to ensure convergence, the global computational cost is increased. Then, we are looking for those methods that do not require time step reductions, consequently reducing the total amount of time step evaluations. In this case, any of the methods shown in Fig. 4(a) need to reduce the time step. Since we do not have any time step reduction and the number of solver iterations per step is stabilized after $t = 1$ for the 32^3 mesh and $t = 1.5$ for the 64^3 mesh, the total amount of accumulated solver iterations (in nonlinear and time loops) shown in Fig. 4 increases almost linearly. We see in this figure that the ASGS scheme performs worse than OSS in this aspect, with a steeper slope in both the 32^3 and 64^3 meshes. With respect to the OSS method, we see that the number of nonlinear iterations needed by the static version of this method results in a steeper slope of the accumulated solver iterations. No significant differences appear between the dynamic linear and nonlinear definitions of the OSS method.

Summarizing, ASGS methods need less nonlinear iterations (due to the treatment of the projections in the OSS method), but on the other hand OSS methods need less solver iterations. Furthermore, *ASGS formulations are prone to instabilities; linear formulations diverge and the nonlinear dynamic formulation requires much more solver iterations*.

We can clearly state that the most efficient method for this setting, in terms of computational cost, is the dynamic (both linear and nonlinear) OSS method; all OSS cases are below ASGS. It has to be said that the dynamic nonlinear OSS case requires less nonlinear iterations in some of the time step computations.

5.2.3. Total energy evolution

In this section we present the total energy evolution of the resolved scales, i.e., the FE component. The results are shown in Fig. 5 for the 32^3 and the 64^3 grids. We observe that all methods have a very similar accuracy for this test case, still far from the DNS result. The difference between the methods becomes even smaller when the mesh is

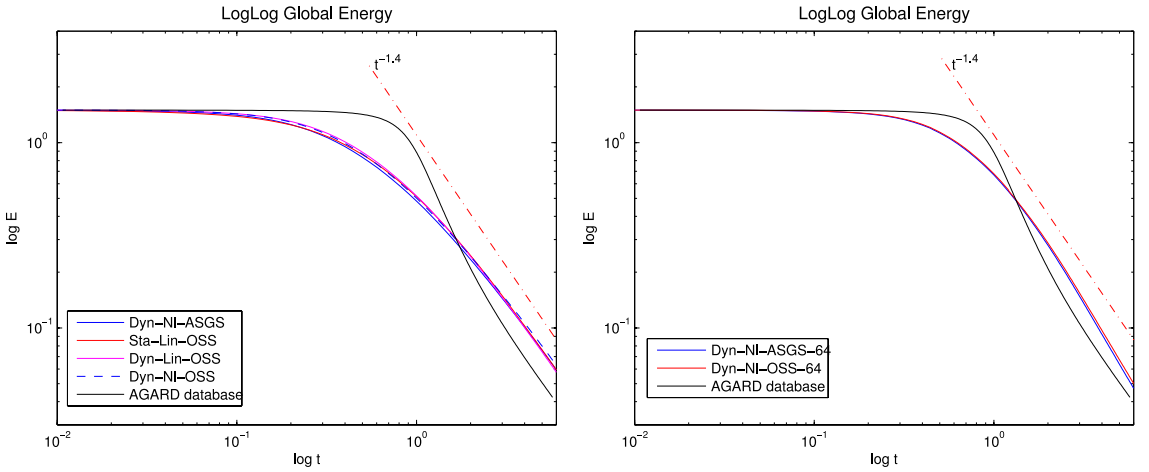

(a) 32^3 mesh. (b) 64^3 mesh.

Fig. 5. Total energy evolution for the 32^3 and 64^3 elements meshes with the scaled initial condition.

refined and they are all closer to the DNS solution. Note that we do not plot the non-converged results from the ASGS static cases.

5.2.4. *Energy spectra*

According to [48], the resolution of the small scales in isotropic decaying turbulence is judged by the shape of the energy spectra at high wave numbers, and requires $k_{\max}\eta \approx 1$, $\eta = (\nu^3/\epsilon)^{1/4}$ being the Kolmogorov length scale and $k_{\max}$ the maximum wave number required. In this case $k_{\max} \approx 182$, which means at least a 300^3 FE mesh for a DNS computation, with a high computational cost. In this section we evaluate the capability of the VMS method to represent the energy of the eddies at the inertial subrange without solving the small scales and compare the results against Kolmogorov's law prediction

$$E(k) \propto \epsilon^{2/3} k^{-5/3},$$

E being the turbulent kinetic energy.

In Fig. 6 the energy spectra for the different cases described in Table 1, using 32^3 and 64^3 linear hexahedral element mesh are presented. We can see in Fig. 6(a) that the energy spectra at $t = 0.2$ decays with a different slope depending on the VMS method used. Although the differences are small and only appear at large wavenumbers, we see that the dynamic OSS models are less dissipative than the Dyn-Nl-ASGS and Sta-Lin-OSS ones. For the finer 64^3 mesh the difference between the spectra obtained using Dyn-Nl-ASGS and Dyn-Lin-OSS are even smaller, as shown in Fig. 6(b); OSS is again less dissipative.

5.2.5. *h–p refinement*

The energy decay computed using 32^3 and 64^3 linear FE meshes is far from the one obtained using DNS [51], as shown in Fig. 5 and discussed above. To make clear that these poor results are due to this crude discretization, we present a mesh refinement analysis, both reducing the element length h and increasing the interpolation order p. We choose the Dynamic and Nonlinear OSS method (Dyn-Nl-OSS), which is the one that shows the lowest slope in the accumulated iterations evolution (Fig. 4) for the 32^3 and 64^3 linear elements mesh. We solve the problem using the discretizations exposed in Table 2.

In Fig. 7 we show the total kinetic energy evolution obtained using the discretizations defined in Table 2. Reducing the mesh size h and/or increasing the polynomial order p (not to be confused with the pressure) the result becomes closer to the DNS, as expected. In Fig. 7(b) three groups can be clearly observed, namely 32 ($Q1$), 32 ($Q2$) and 64 ($Q1$) and the remaining three. The best results are obtained using $Q2$ elements although the difference is really small.

Given the differences in the total energy evolution the time at which the $k^{-5/3}$ law is achieved differs for the different methods. We show the energy spectra at time $t = 0.8$ and $t = 1.0$ for the different cases presented before in Fig. 8. As it can be observed in Fig. 8(a), at $t = 0.8$, only the energy spectra obtained using the 32 ($Q1$) and 64

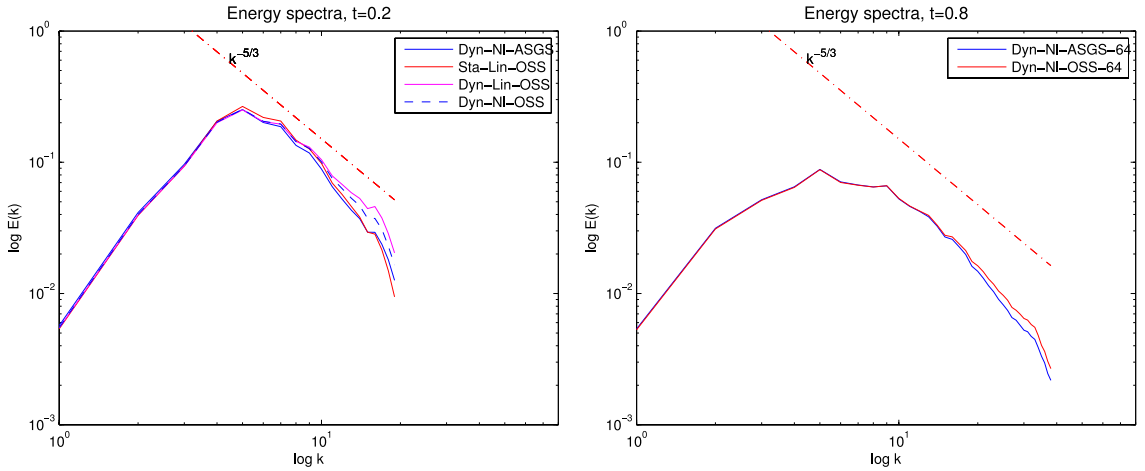

(a) 32^3 mesh. (b) 64^3 mesh.

Fig. 6. Energy spectra at $t = 0.2$ (32^3 mesh) and $t = 0.8$ (64^3 mesh).

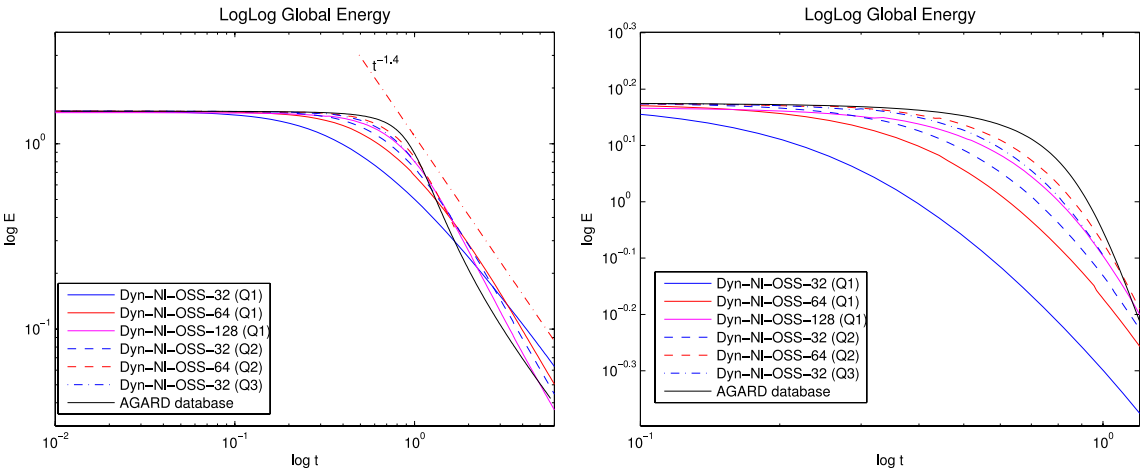

(a) Total evolution. (b) Close up view.

Fig. 7. Total kinetic energy evolution.

Table 2
h–p refinement cases.

Label	Mesh elements	Element type
32 ($Q1$)	32^3	Hexahedral linear ($Q1$)
64 ($Q1$)	64^3	Hexahedral linear ($Q1$)
128 ($Q1$)	128^3	Hexahedral linear ($Q1$)
32 ($Q2$)	32^3	Hexahedral quadratic ($Q2$)
64 ($Q2$)	64^3	Hexahedral quadratic ($Q2$)
32 ($Q3$)	32^3	Hexahedral cubic ($Q3$)

($Q1$) have a steeper slope, while the other cases are almost parallel to the $k^{-3/5}$ line. This is what was expected since the kinetic energy decay occurs earlier in the coarser cases. In Fig. 8(b) we show the energy spectra at $t = 1.0$, and compare it against the DNS spectrum from [51] at the same time step. It can be observed that the results tend to the DNS one as we increase resolution, being the $64(Q2)$ case the most accurate one.

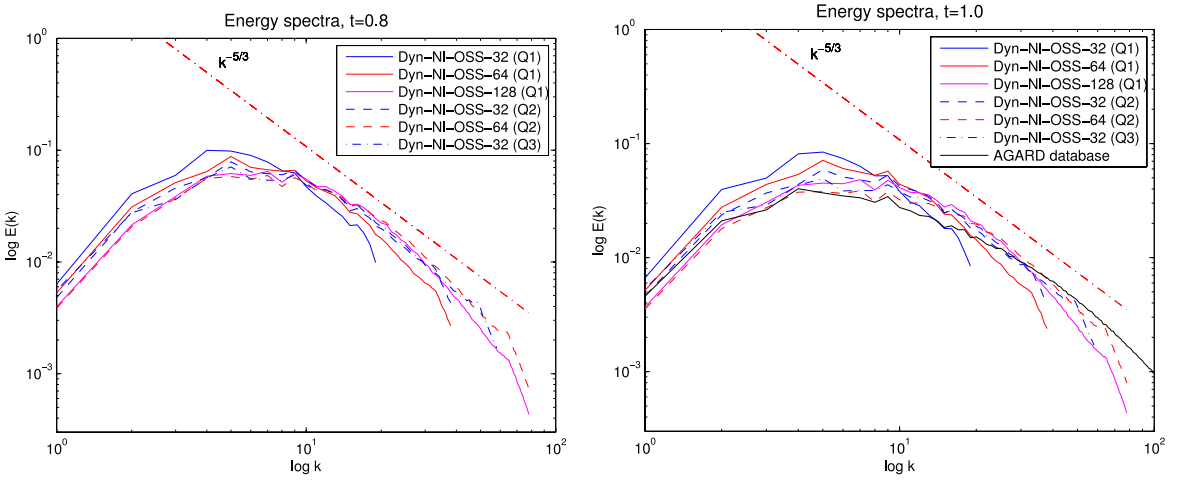

(a) Energy spectra at $t = 0.8$.

(b) Energy spectra at $t = 1.0$.

Fig. 8. Energy spectra at $t = 0.8$ and $t = 1.0$ for the h–p refinement defined in Table 2.

Note that the DNS spectra is not present in Fig. 8(a) because it is not available in the database [51] at this time step.

6. Taylor–Green vortex

6.1. Problem definition

The Taylor–Green vortex (TGV) problem is a typical and widely used problem in turbulence numerical simulations. This problem aims to show, in a relatively simple flow, the basic turbulence decay mechanisms like the turbulent energy cascade, the production of small eddies and the enhancement of dissipation by the stretching of vortex lines.

6.1.1. Initial condition

As in the previous example, the computational domain is the unit cube with periodical boundary conditions. The initial analytical condition for this problem, unlike the DHIT problem, is defined in the physical space (see, e.g., [58]), and given by

$$\begin{aligned} u_x &= u_0 \cos(x) \sin(y) \sin(z), \\ u_y &= -u_0 \sin(x) \cos(y) \sin(z), \\ u_z &= 0, \\ p &= p_0 + \frac{1}{16} \left(\cos(2x) + \cos(2y)\right) \left(\cos(2z) + 2\right), \end{aligned} \tag{56}$$

with

$$u_0 = \frac{2}{\sqrt{3}} \sin\left(\gamma + \frac{2\pi}{3}\right).$$

We choose $\gamma = 0$, which gives the mean initial velocity $u_0 = 1$. The initial velocity field on the Fourier space has eight modes located at the wave numbers $\mathbf{k} = (\pm 1, \pm 1, \pm 1)$, which means that the initial flow generates a single vortex scale. The pressure constant parameter p_0 is chosen equal to zero.

6.1.2. Setting

We solve the TGV problem using a Reynolds number $\mathrm{Re} = 1600$. The most common Reynolds numbers available in the literature are $\mathrm{Re} = 800$, $\mathrm{Re} = 1600$ and $\mathrm{Re} = 3000$ (see, e.g., [40,58–60]). We use the same VMS methods as for the DHIT problem defined in Section 5 to solve this test, namely the ASGS and OSS methods, both with

linear and nonlinear definitions of the convective term and static or dynamic tracking in time of the subscales, as it is summarized in Table 1. The stabilization parameters for each method are the same as those chosen for the DHIT test, see Section 5.1.2, and discussed in Section 8.

Initially we consider a mesh of 32^3 hexahedral linear elements ($Q1$), but we will redefine this discretization to analyze the method performance when we refine the mesh, decreasing the element size h or increasing the degree of the interpolation polynomial p. It implies to solve the problem on meshes with 64^3 and 128^3 linear ($Q1$), quadratic ($Q2$) or cubic ($Q3$) hexahedral elements. We also use a $20^3(Q3)$ discretization to compare against other authors results.

6.2. Numerical results

6.2.1. Vorticity

The TGV test is characterized by its laminar evolution at the initial time steps, when the flow is strongly anisotropic due to the structured large-scale vortices directly related to the initial condition. If the Reynolds number is large enough, the vortex-stretching process, which activates the energy cascade effect, transfers energy from large to small-scales and the flow becomes unstable and turbulent. According to Brachet et al. [61], the flow becomes nearly isotropic for $\mathrm{Re} \geq 1000$.

In Fig. 9 we present some vorticity isosurface images showing this process for a 128^3 linear hexahedral elements mesh, for the dynamic and nonlinear OSS method. Note that the initial condition (Fig. 9(a)) consists in eight vortices with the same scale corresponding to the eight Fourier modes located at $\mathbf{k} = (\pm 1, \pm 1, \pm 1)$, as it has been pointed out previously.

6.2.2. Comparison of VMS methods

In order to compare the different VMS methods defined previously and to test their performance as LES models we solve the TGV test on a 32^3 and 64^3 linear elements mesh with a Reynolds number $\mathrm{Re} = 1600$. As for the DHIT test, the results obtained using the different methods listed in Table 1 are very similar for these coarser discretizations. The only point that is worth noting is that the linear and static ASGS case (Sta-Lin-ASGS) and the dynamic and linear ASGS case (Dyn-Lin-ASGS) diverge at some time step before $t = 9$. Anyway, all the methods converge as $h \to 0$ and the accuracy depends much more on the mesh size than on the choice of the method. In turn, similar trends for the computational cost analyzed in the previous section have been observed.

6.2.3. h–p refinement

As in the DHIT problem, we perform a refinement study reducing h and/or increasing p using Dyn-Nl-OSS. The global energy evolution and the energy spectra are shown in Fig. 10. Fig. 10(a) displays the total kinetic energy evolution compared with the DNS [61]. The results show that all cases, excluding the 32^3 and 64^3 linear hexahedral meshes, follow almost perfectly the line defined by the DNS result points. On the other hand, Fig. 10(b) displays the energy spectra at $t = 9$, when the dissipation is maximum and the flow is evolving to turbulence. We compare the energy spectra obtained solving all the cases considered before with the DNS computed by [58], using the same Reynolds number ($\mathrm{Re} = 1600$) at the same time.

In Fig. 11 we show the dissipation rate of the problem, compared to the DNS results. The dissipation rate is directly related to the enstrophy of the problem, $\epsilon = 2\nu \left(\frac{1}{2} \left\langle |\omega|^2 \right\rangle \right)$, where $|\omega|$ is the modulus of the vorticity. At the continuous level, it determines the kinetic energy decay which, at the discrete level, is also influenced by the numerical dissipation (see Eq. (35)). When an explicit model is used, the dissipation introduced by the subgrid model also needs to be included. The FE viscous dissipation $\nu \|\nabla \mathbf{u}_h\|^2$, is shown in Fig. 11(a) whereas the total dissipation rate $\nu \|\nabla \mathbf{u}_h\|^2 + \varepsilon_h$ defined by Eq. (35) is shown in Fig. 11(b).

As in the DHIT problem, the results obtained using the coarser $32^3(Q1)$ and $64^3(Q1)$ meshes are not accurate, the FE viscous dissipation being far from the exact viscous dissipation, as shown in Fig. 11(a). The total dissipation introduced by the method is too large and, especially for the $32^3(Q1)$, peaked at earlier times, i.e., the energy decays faster and earlier than it should (see Fig. 11(b)). When finer resolutions are used, the flows dynamics are much better predicted. Even when the resolution is not enough to completely capture the viscous dissipation, the total dissipation compares very well with the exact one, as shown in Fig. 11. This is a *clear illustration of the very good performance of the method, which adds the right amount of dissipation when the gradients are not captured by the resolution*.

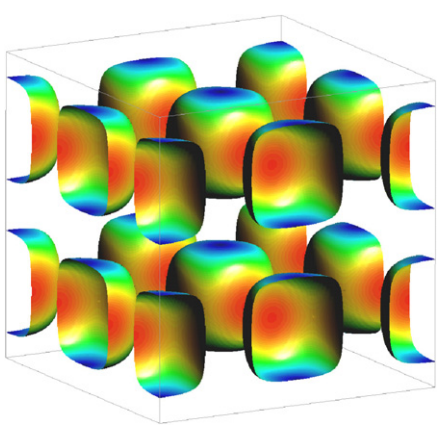

(a) Isosurface for $|\omega| = 1.0$ at $t = 0.0$.

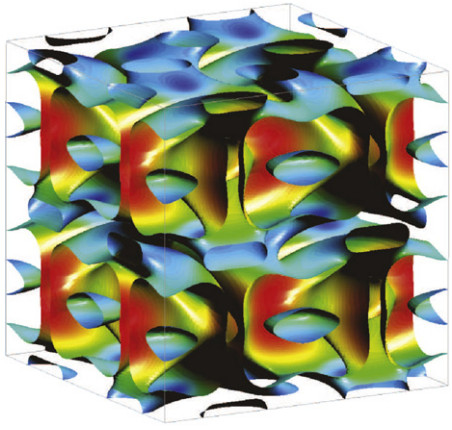

(b) Isosurface for $|\omega| = 1.0$ at $t = 2.0$.

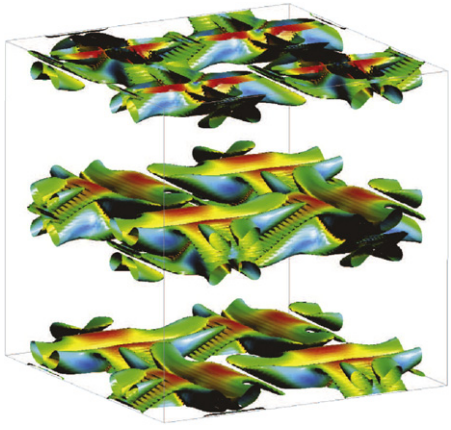

(c) Isosurface for $|\omega| = 2.5$ at $t = 4.1$.

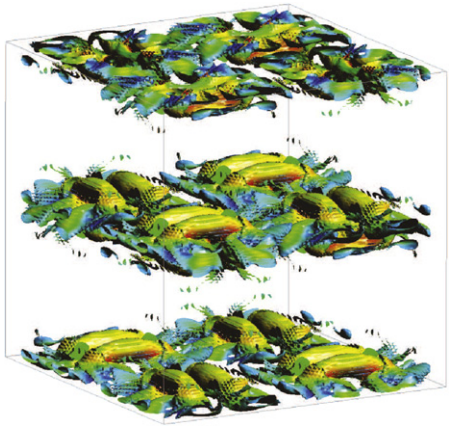

(d) Isosurface for $|\omega| = 5.0$ at $t = 6.1$.

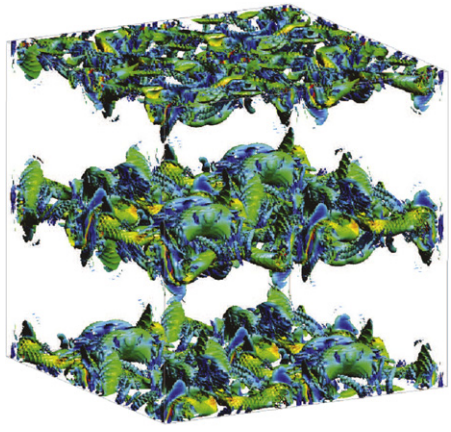

(e) Isosurface for $|\omega| = 8.0$ at $t = 8.2$.

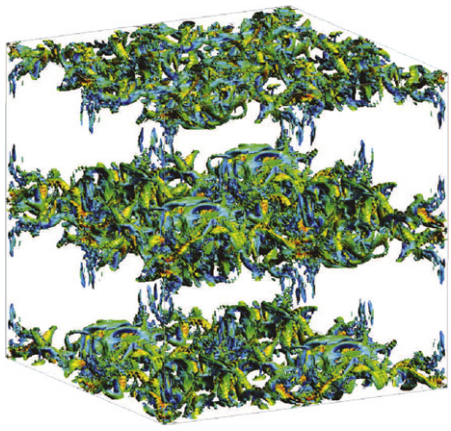

(f) Isosurface for $|\omega| = 9.0$ at $t = 10.2$.

Fig. 9. Vorticity isosurfaces with velocity contour at different time steps.

6.2.4. Comparison with a non-stabilized method

All the results presented up to this point have been computed using a VMS method, either ASGS or OSS. But, what would be the result using other methods? Are the methods presented here, comparable to classical LES methods?

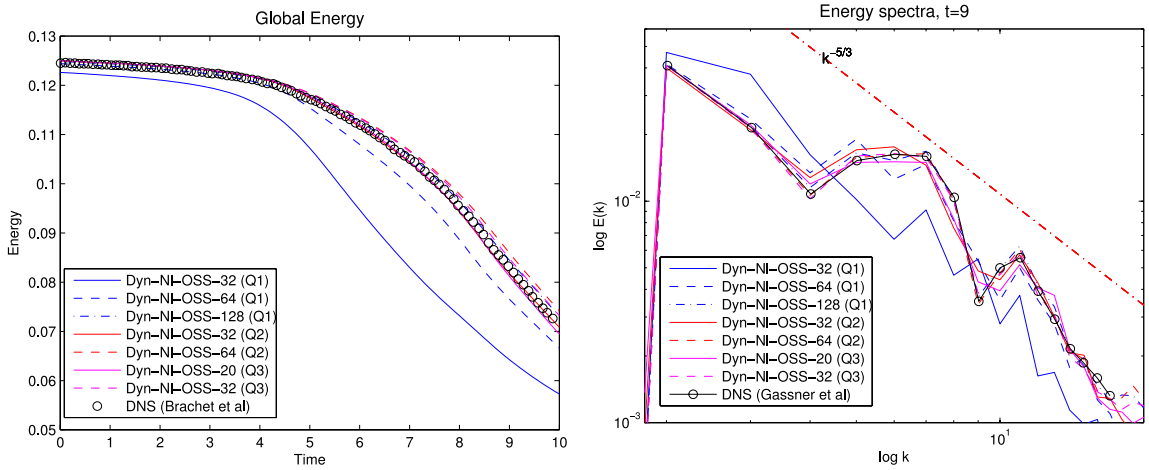

(a) Total kinetic energy evolution. (b) Energy spectra at $t = 9$.

Fig. 10. Total kinetic energy evolution and energy spectra for the $h-p$ refinement cases.

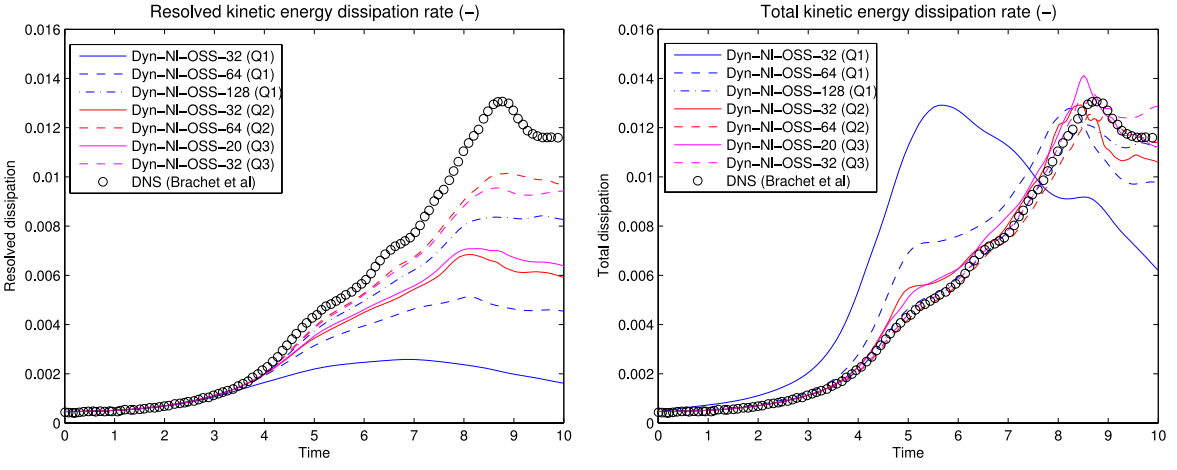

(a) Resolved. (b) Total.

Fig. 11. Dissipation rate evolution for the $h-p$ refinement cases.

Which methods perform better? To answer all these questions, we compare the results obtained here against those obtained using the dynamic Smagorinsky model [40] and the adaptive local deconvolution method [41] specifically designed as an implicit LES model. The former has been obtained with a filter of size $2\pi/64$ and spectral resolution up to $2\pi/256$, thus not having numerical but only modeling error. In turn, the latter has been obtained using a 64^3 grid without explicit subgrid model, an explicit third-order Runge–Kutta scheme for the time discretization, a fourth order spatial approximation of the symmetric terms and its particular approximation of the convective term which is based on the (fourth order) five-point central stencils approximation of the convective term [41]. To make the comparison as fair as possible we select those combinations of h and p that result in a similar number of degrees of freedom, which are $64^3(Q1)$ (second order), $32^3(Q2)$ (third order) and $20(Q3)$ (fourth order) meshes (the last one having actually a bit less degrees of freedom).

The FE viscous dissipation is shown in Fig. 12(a) compared to the resolved dissipation obtained using the dynamic Smagorinsky model [40] and the "molecular dissipation" of [41] (the one computed using the molecular viscosity and the approximated solution, equivalent to our FE viscous dissipation but in the finite volume context). The total dissipations of the three methods are compared in Fig. 12(b).

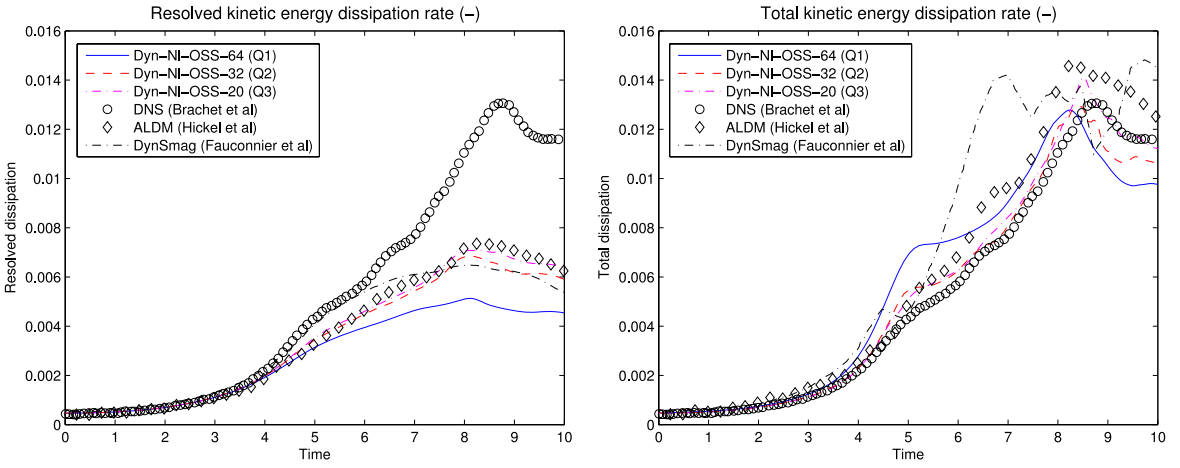

(a) Resolved. (b) Total.

Fig. 12. Dissipation rate evolution compared to the dynamic Smagorinsky [40] and ALDM models [41].

It can be observed in Fig. 12(a) that all the methods produce similar results, The dynamic Smagorinsky is more accurate in predicting the resolved dissipation at earlier times (up to $t \approx 6$) but less accurate at later times (see Fig. 12(a)). We plot the total dissipation in Fig. 12(b). We can see the excellent job our implicit LES model does when the 20($Q3$) mesh is used, which would result in an excellent prediction of the resolved kinetic energy decay (which is not available in [41]).

7. Turbulent channel flow

After studying the performance of VMS in the LES of homogeneous flows we turn our attention to wall-bounded turbulent flow and present results of fully developed turbulent flow in a channel.

7.1. Problem definition

This test consists of a fluid that flows between two parallel walls driven by an imposed pressure gradient which is defined by the Reynolds number based on the wall shear velocity, Re_τ. In the important amount of literature devoted to this problem, the usual Reynolds numbers are: $\mathrm{Re}_\tau = 590$, $\mathrm{Re}_\tau = 395$ and $\mathrm{Re}_\tau = 180$ (see [12,15,18,24,34–36, 62–64]). We will restrict our attention to $\mathrm{Re}_\tau = 180$ and $\mathrm{Re}_\tau = 395$.

7.1.1. Computational domain and mesh definition

We consider a computational domain defined by a box of length ($L_x \times L_y \times L_z$), which depends on the Reynolds number. For $\mathrm{Re}_\tau = 180$ the domain size is ($4\pi\delta \times 2\delta \times 4/3\pi\delta$) while for $\mathrm{Re}_\tau = 395$ the size of the channel is ($2\pi\delta \times 2\delta \times 2/3\pi\delta$). The x-direction is the flow direction, also called streamwise direction, the y-direction is the wall-normal direction, and the z-direction is the spanwise direction. In Fig. 13 we show schematically the geometry of the computational domain for this test.

In the wall-normal direction boundaries ($y = -\delta$ and $y = \delta$) we impose a non-slip condition. The streamwise and spanwise directions are assumed to be homogeneous, so we use periodic boundary conditions in these directions.[3]

We solve the problem using the coarsest mesh from previous tests, 32^3 linear hexahedral ($Q1$) elements. The refinement in the wall-normal direction follows a hyperbolic function, also used in [24,34–36,62], defined as

$$y_i = \frac{\tanh\left(\gamma\left(\frac{2i}{np_y} - 1\right)\right)}{\tanh(\gamma)},$$

[3] According to Kim et al. [63], the use of periodic boundary conditions in the homogeneous directions can be justified when the computational box is such that the largest eddies in the flow fit in the computational domain. This is the case considered here.

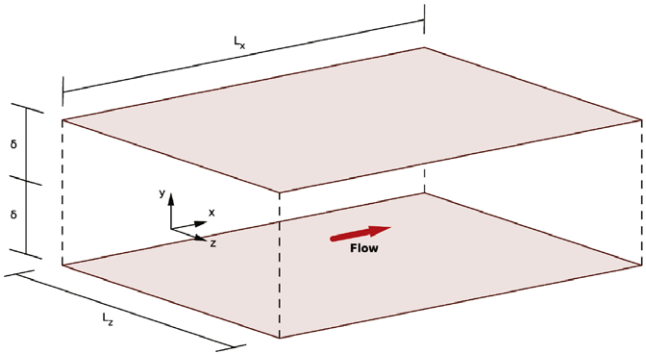

Fig. 13. Channel computational domain.

Table 3
Test parameters for the different friction Reynolds number.

Re_τ	180	395
ν	$3.5714 \cdot 10^{-4}$	$1.4545 \cdot 10^{-4}$
u_τ	$6.4286 \cdot 10^{-2}$	$5.7455 \cdot 10^{-2}$
τ_w	$4.1327 \cdot 10^{-3}$	$3.3010 \cdot 10^{-3}$
f_x	$4.1327 \cdot 10^{-3}$	$3.3010 \cdot 10^{-3}$
δt	0.06	0.03

where $i = 1, \ldots, np_y$ with np_y the total amount of nodes in the wall-normal direction. Here, γ is chosen to be equal to 2.75 for both $\mathrm{Re}_\tau = 180$ and $\mathrm{Re}_\tau = 395$. We refer the reader to [65] for a complete study of the influence of the discretization in the results of the TCF.

7.1.2. Setting

As it has been said above, we solve the problem using two different friction Reynolds numbers, $\mathrm{Re}_\tau = 180$ and $\mathrm{Re}_\tau = 395$. We compare our results against those obtained by DNS in [63,64] and we choose our parameters accordingly. We take the bulk mean velocity and the half channel height equal to one, $\bar{U} = 1$ and $\delta = 1$. The viscosity is computed from the estimated Reynolds number based on the bulk mean velocity Re. Then, from the friction Reynolds number Re_τ we compute the friction velocity (u_τ), the wall shear stress (τ_w) and a driving force equivalent to a pressure gradient (f_x), given by [66]:

$$u_\tau = \frac{\nu \mathrm{Re}_\tau}{\delta}, \qquad \tau_w = \rho u_\tau^2, \qquad f_x = \frac{\tau_w}{\delta}.$$

We use the Crank–Nicolson time integration scheme with a constant time step. Ham et al. test in [67] the influence of the time step for a fully implicit Finite Difference midpoint method, equivalent to Crank–Nicolson, on the statistics of a TCF DNS. They found little variation in statistical turbulence quantities up to $\delta t^+ = 1.6$. Following Gravemeier et al. [35], we define a time step in wall units $\delta t^+ = \frac{\delta t u_\tau^2}{\nu} \approx 0.69$, which, according to [67], should not affect the turbulent quantity statistics. The same authors performed 25 000 time steps in order to allow the flow to develop and they collected the statistics during another 5000 time steps. A total averaging time about $500\delta/U_0$ is used in [68] once the statistically stable regime is achieved.

In Table 3 we present the value of the different parameters defined above for the two different friction Reynolds numbers. For the initial condition we impose a parabolic profile obtained solving the stationary Stokes problem with the driving force and viscosity defined above. Additionally, with the aim to achieve a fully developed flow earlier, we introduce a perturbation with a maximum value of 10% the bulk velocity.

Our purpose is to check the VMS methods defined in Section 2.2 for a wall-bounded flow. Following the computations performed for the previous tests, we solve the problem using the same cases defined in Table 1 and the numerical parameters $\tau_c = 0$ and τ_m are defined in the same way, now with the algorithmic constants $c_1 = 12$ and $c_2 = 8$ (see Section 8) and the characteristic length, h, is chosen to be the minimum element length.

7.2. Numerical results

7.2.1. Velocity profiles

We first present the mean streamwise velocity profile scaled by the wall shear stress velocity, $\langle u \rangle^+ = \frac{\langle u \rangle}{u_\tau}$ for all cases defined in Table 1, where $\langle \cdot \rangle$ denotes the mean value in streamwise and spanwise directions and in time, as a function of $y^+ = \frac{y u_\tau}{\nu}$.

In Fig. 14(a) we show the mean streamwise velocity normalized by the wall-shear velocity, u_τ, obtained for all cases considered in Table 1 in a 32^3 linear elements mesh for the $\mathrm{Re}_\tau = 395$ case. We compare the results with the DNS one obtained in [64]. We can observe in Fig. 14(a) that all methods perform quite similar and are very close to the DNS result. Fig. 14 also depicts the streamwise, spanwise and wall-normal root mean square (rms) velocity fluctuation components normalized by the wall-shear stress velocity.

7.2.2. Reynolds shear stress

Another turbulent quantity widely used in the TCF test is the Reynolds shear stress. At the continuous level the Reynolds shear stress is defined as

$$R_{xy} = -\left\langle u' v' \right\rangle + \nu \frac{\partial \langle u \rangle}{\partial y}, \tag{57}$$

being u and v the velocity in the streamwise direction and the wall-normal direction, respectively, and the prime denoting the fluctuations, i.e., the variable minus the mean.

It can be seen that for the discrete equation (13), one can obtain the Reynolds shear stress defined as follows:

$$R_{xy} = -\left\langle a_x' a_y' \right\rangle + \nu \frac{\partial \langle u_h \rangle}{\partial y} = \underbrace{-\left\langle u_h' v_h' \right\rangle}_{\mathrm{I}} \underbrace{-\left\langle u_h' \tilde{v}' \right\rangle - \left\langle \tilde{u}' v_h' \right\rangle - \left\langle \tilde{u}' \tilde{v}' \right\rangle}_{\mathrm{II}} + \underbrace{\nu \frac{\partial \langle u_h \rangle}{\partial y}}_{\mathrm{III}} \tag{58}$$

being a_i the ith component of the advection velocity. In (58) we have used the nonlinear definition of the advection velocity defined in (25).

The first term on the second part of (58) (term I) is the contribution of the resolved scales (FE component) to the cross term $\left\langle a_x' a_y' \right\rangle$. Term II denotes the contribution of the subgrid scales and their interaction with the FE components, that is, the unresolved part of the equation. Finally, term III accounts for the viscous portion of the Reynolds shear stress. Note that the derivatives of the approximated subscales are not computable, since these approximated subscales are discontinuous and have been designed to approximate the effect of the exact subscales on the FE scales elementwise.

For a fully developed and statistically stable turbulent flow, the Reynolds shear stress along the wall-normal direction has a linear shape (see [63]). Normalized by the viscous term III value at the wall, the total Reynolds shear stress in terms of y/δ should have the following expression: $R_{xy}(y/\delta) = (-y/\delta)$. Fig. 15 depicts the absolute value of the Reynolds shear stress along the upper half channel ($y > 0$), with the different terms appearing in (58) and compared with the DNS in [64], for the Dyn-Nl-OSS case with $\mathrm{Re}_\tau = 395$. The computed results are almost identical to the DNS ones. It has to be noted that the computed results are evaluated at the integration points due to the presence of the derivative in the Reynolds shear stress, which using linear FEs is constant at each element. Then, using two integration points per direction for the numerical integration, term III will be constant for those two integration points being in the same element. This behavior is observed in Fig. 15, where the viscous term is pairwise constant. This last fact also affects the total Reynolds shear stress. Since the resolved term has different values at each element Gauss point, the sum of terms I and III results in an oscillatory shape near the wall, where the viscous term is more relevant. It is also seen that the unresolved term II does not contribute to the Reynolds shear stress, which is a good property of the tested VMS methods. The results for the remaining cases in Table 1 are similar to those presented in Fig. 15 and have not been reported.

8. Sensitivity with respect to the stabilization parameters

All the VMS models considered herein depend on the stabilization parameters τ_m and τ_c, which contain constants c_1 and c_2 whose value is chosen from numerical experiments. However, we can infer from (38) or (39) how this

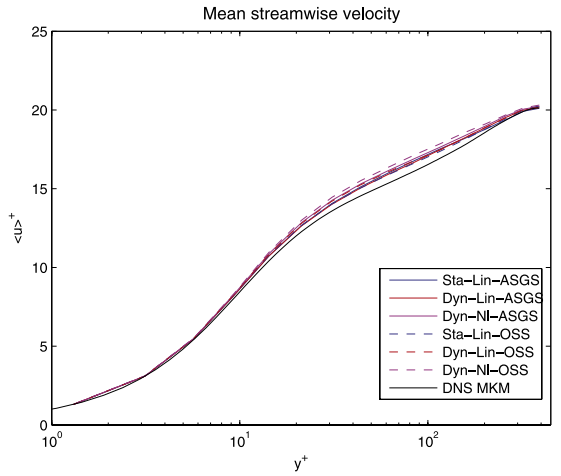

(a) Mean streamwise velocity.

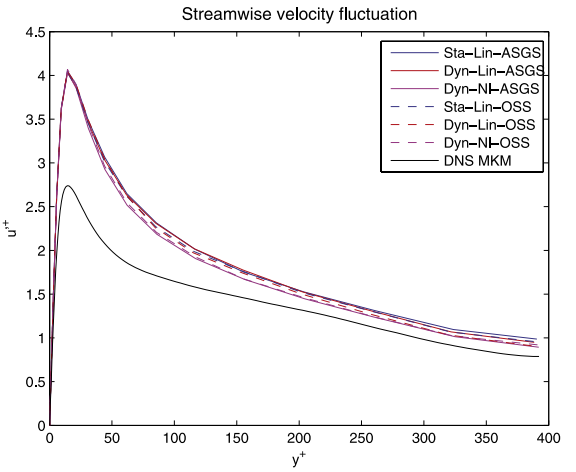

(b) Rms streamwise velocity fluctuation.

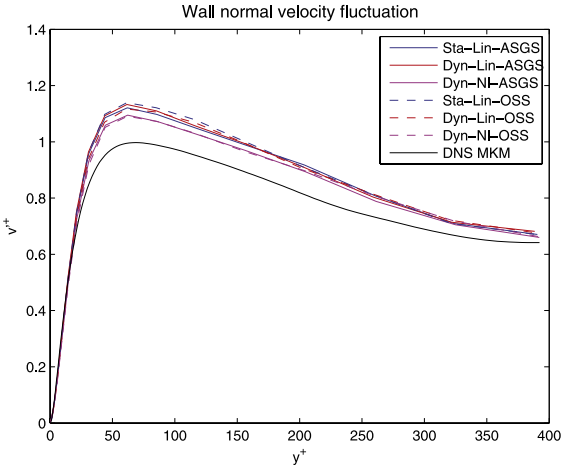

(c) Rms wall-normal velocity fluctuation.

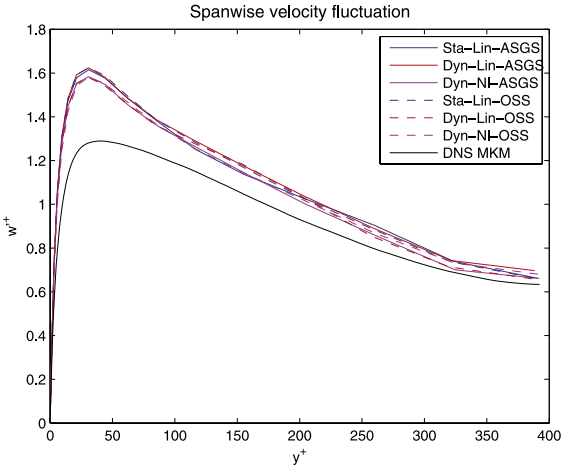

(d) Rms spanwise velocity fluctuation.

Fig. 14. Mean streamwise velocity and rms velocity fluctuations for $\mathrm{Re}_\tau = 395$ case using a 32^3 $Q1$ mesh.

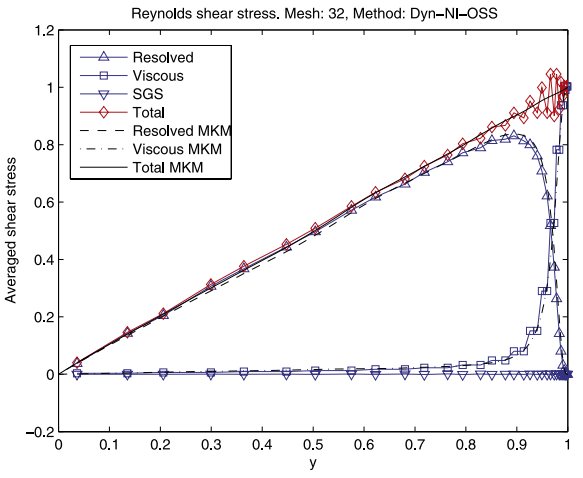

Fig. 15. Reynolds stress of the Dyn-Nl-OSS case.

dependency will be. As mentioned before, the last two terms in (39) are dissipative and therefore, increasing τ_m and/or τ_c we obtain a more dissipative method. From (20)–(21), increasing τ_m results in a reduction of τ_c. More precisely

$$\tau_c = \nu + \frac{c_2}{c_1}|\mathbf{a}|h \tag{59}$$

from where we see that increasing c_1 reduces both τ_m and τ_c but increasing c_2 reduces τ_m but increases τ_c. On the other hand, only the fourth term in (39) is essential to control $\tau_m \|\mathcal{P}(\mathbf{a}\cdot\nabla\mathbf{u}_h + \nabla p_h)\|^2$ and it is possible to choose $\tau_c = 0$.

The results presented above have been obtained using different settings of the numerical stabilization parameters τ_m and τ_c. In DHIT and TGV tests, we take the algorithmic constants $c_1 = 12$ and $c_2 = 2$ for τ_m and we set $\tau_c = 0$, while for the TCF test we have used $c_1 = 12$ and $c_2 = 8$ for τ_m and also $\tau_c = 0$. In this section we analyze the influence of these parameters on the numerical results and justify our choice of the constants for the large eddy simulation of turbulent flows.

We have performed a sensitivity analysis of the VMS schemes with respect to the value of c_1 and c_2. To see the effect of such algorithmic constants on τ_m and τ_c independently, we define a new constant c_c which allows us to redefine (59) as

$$\tau_c = c_c\left(\nu + \frac{c_2}{c_1}|\mathbf{a}|h\right). \tag{60}$$

These experiments have been done for the DHIT test using the Dyn-Nl-OSS case in a 32^3 $Q1$ mesh and the results are depicted in Fig. 16. They show important changes in the dissipation the VMS methods introduce when constants are changed. It is known that the decay rate of kinetic energy in isotropic turbulence is driven by large scales (of the order of the integral scale) (see, e.g., [69]). As we have observed, the subgrid model has only influence when a very coarse grid is used.

In particular, for high Reynolds number problems, the constant c_1 does not have so much influence on τ_m, but it does on τ_c. With respect to c_2, we observe that it influences the energy dissipation of the method, which is increased when the value of this constant is decreased. When τ_c is activated ($c_c = 1$), we observe a growth of the energy dissipation when the coefficient c_2/c_1 increases. This behavior is what we are expecting since the method becomes more diffusive when τ_c is increased due to the last term in (39).

Concerning the energy spectra, it is also shown in Fig. 16(a) and (b) that the only constant that influences the result when $\tau_c = 0$ is c_2. In these figures we can see that when we increase c_2 the method is less dissipative, resulting in an inappropriate slope of the energy spectra. We can observe that with $c_2 = 2$ the decay of the energy behaves correctly, keeping the $k^{-5/3}$ law. For the largest values of c_2 the energy at small scales is not properly dissipated. Note that for $c_2 = 2$ the slope of the energy spectrum is kept almost constant along the time, which does not happen in the other cases. When we activate τ_c (see Figs. 16(c) and (d)) we are introducing additional dissipation into the system that eliminates the pile up of the energy spectra for all the cases, but generally results in steeper slopes. Here we also have to note that the energy spectra slope is time dependent for all cases except for $c_2 = 2$. This analysis led us to choose $c_1 = 12$ and $c_2 = 2$ for τ_m and set $\tau_c = 0$ for homogeneous turbulence, i.e., DHIT and TGV tests.

In order to go in depth on the effect of the algorithmic constants c_1 and c_2 and the stabilization parameter τ_c of the incompressibility equation, we compare the results for the TCF problem with a friction Reynolds number $\mathrm{Re}_\tau = 180$ using the same choice made for homogeneous turbulence ($c_1 = 12,\ c_2 = 2$ and $\tau_c = 0$) against the setting of the incompressible case in [65] ($c_1 = 12,\ c_2 = 2$ and τ_c as in (21)) and a less dissipative setting with $c_1 = 12,\ c_2 = 8$ and $\tau_c = 0$. These tests have been done using the Dyn-Nl-OSS case in a 32^3 $Q1$ mesh.

In Fig. 17(a) the mean velocity in the streamwise direction is shown. As in the case of homogeneous turbulence, some differences between the three cases can be observed, the choice used in Section 7 being the most accurate one. The effect of the algorithmic constant c_2 and the stabilization parameter τ_c in the problem solution can be clearly observed, i.e., the less dissipative choice gives the best results. Figs. 17(b)–(d) depict the rms velocity fluctuations in all directions. The fluctuations in the streamwise direction are better predicted using ($c_1 = 12,\ c_2 = 8$ and $\tau_c = 0$) but the spanwise and wall-normal directions are not.

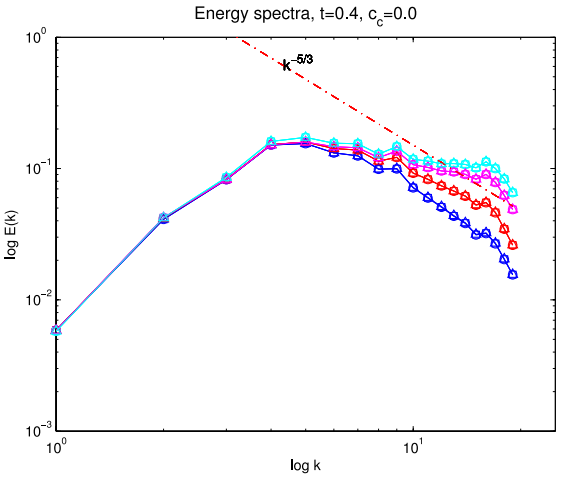

(a) Energy spectra at $t = 0.4$ with $c_c = 0$.

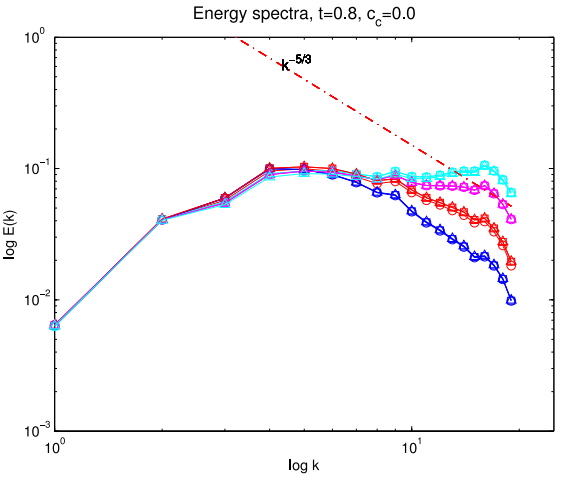

(b) Energy spectra at $t = 0.8$ with $c_c = 0$.

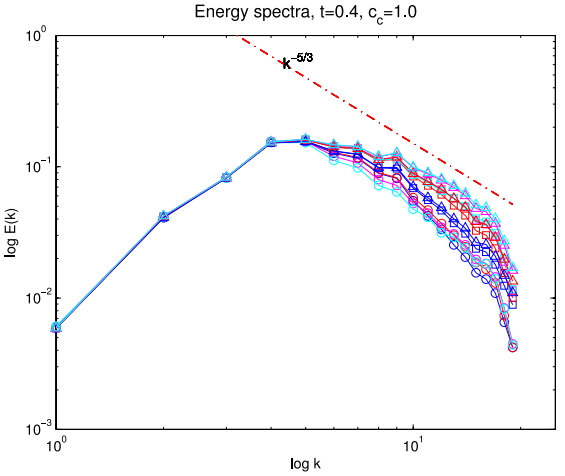

(c) Energy spectra at $t = 0.4$ with $c_c = 1$.

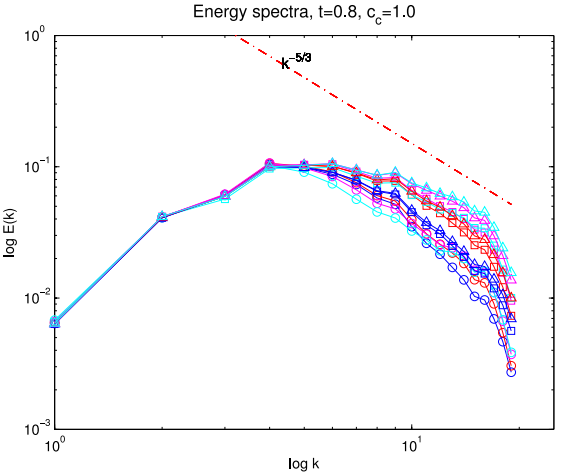

(d) Energy spectra at $t = 0.8$ with $c_c = 1$.

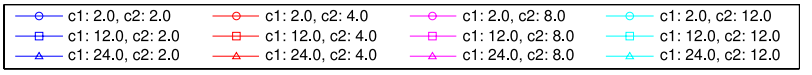

(e) Legend.

Fig. 16. Comparison of energy spectra for different c_1, c_2 and c_c in the DHIT test.

9. Behavior in the small time step limit

Small time step instabilities for VMS LES simulations of turbulent flows have been reported in [24,39]. In these references, the VMS models differ from the ones in this work. Instead of the definition of τ_m in (20), a time step dependent stabilization parameter τ_m

$$\tau_m = \left(\frac{1}{\delta t} + \frac{c_1 \nu}{h^2} + \frac{c_2 |\mathbf{a}|}{h} \right)^{-1},$$

is considered in all cases.[4] The plain introduction of a time step dependency in τ_m faces serious difficulties:

[4] The parameter $\tau_{m,t}$ for the dynamic subscales model also scales with δt, as discussed in Section 4. *However*, this dependence comes from a consistent time integration of the subscale time derivative (see also [22, Section 3.2]).

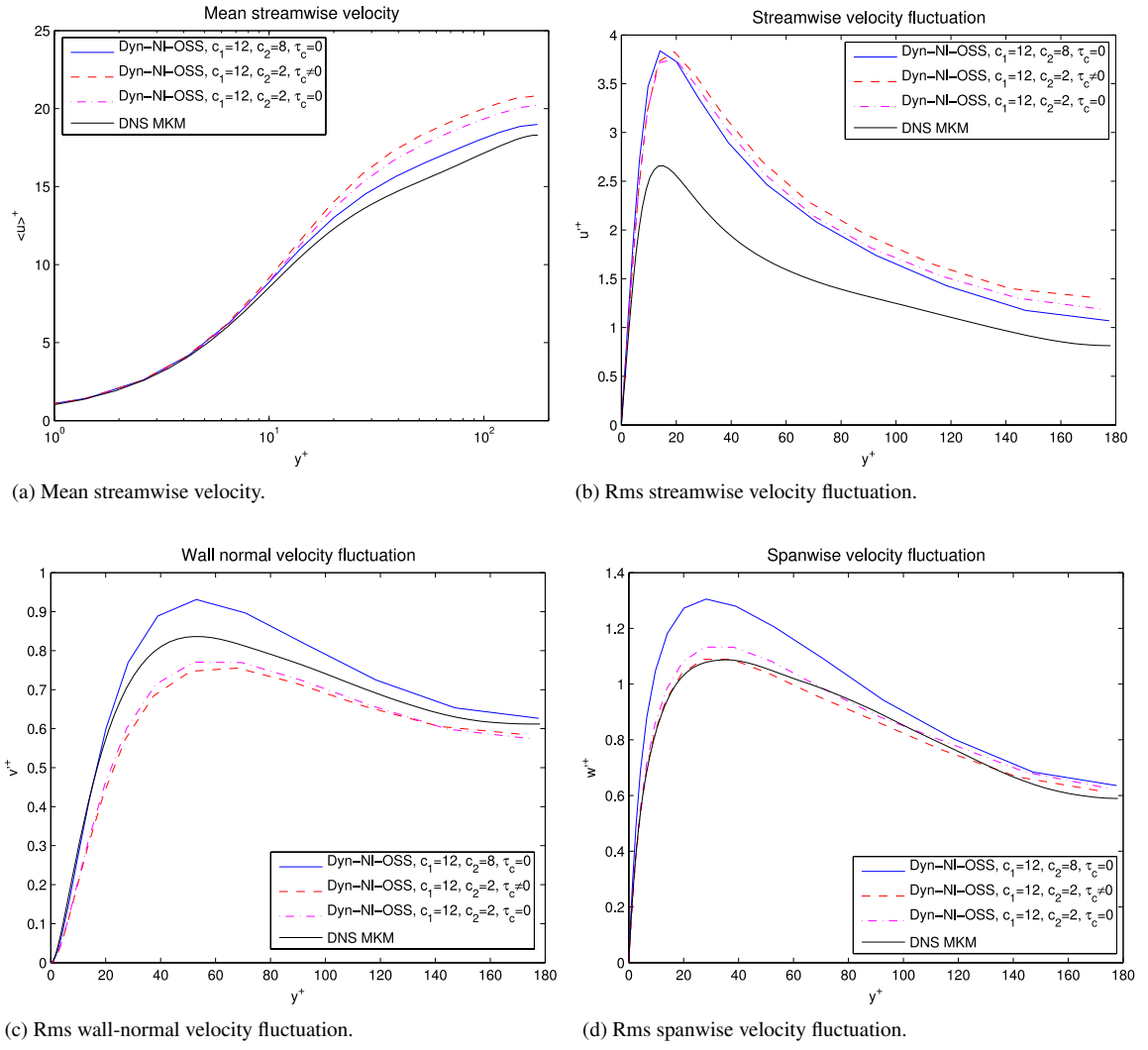

(a) Mean streamwise velocity.

(b) Rms streamwise velocity fluctuation.

(c) Rms wall-normal velocity fluctuation.

(d) Rms spanwise velocity fluctuation.

Fig. 17. Comparison of mean streamwise velocity and rms velocity fluctuations for $\mathrm{Re}_\tau = 180$ case using a 32^3 $Q1$ mesh.

- The method becomes unstable in the small time step limit since it converges to the unstable Galerkin formulation.
- If τ_c is computed from (21) (as it is usually done, see, e.g., [18,24,35,39]), $\tau_m \sim \delta t$ and $\tau_c \sim \delta t^{-1}$ in the small time step limit. If this approach is followed, the essential numerical dissipation given by the fifth term in (38) is reduced as $\delta t \to 0$, whereas the numerical dissipation introduced by the last term on the left hand side (a incompressibility penalty term) of (38) is increased. It has a compensating effect in practice, but the penalty term does not properly act as a turbulence model.

Let us perform a test to study the small time step behavior of the VMS methods presented in Section 2, using the skew-symmetric *type* 1 form of the convective term, as in previous numerical experiments. We also include a combination we do not advocate here, static subscales and nonlinear splitting, an approach followed in [17,18,24,35,39]. The behavior of all the methods for the TCF test with $\delta t = 0.002$ is summarized in Table 4, where YES means that the simulation was successful, NO means that the simulation diverged and $\delta t \downarrow$ means that the simulation was successful only when the adaptive time step strategy described in Section 5.1.2 was used.

It is important to note that the static and nonlinear ASGS formulation used in [18,24,35,39] with the convective term *type* 2 becomes unstable after some time, as also reported in these works, even for the time step size defined in Section 7.1.2. However, using the skew-symmetric *type* 1 form of the convective term, which exactly conserves energy, the simulation ended successfully for the time step defined in Section 7.1.2, but failed to converge with the small one.

Table 4
Small time step convergence analysis.

Method	ASGS				OSS			
Tracking	Static		Dynamic		Static		Dynamic	
Advection	Linear	Nonlinear	Linear	Nonlinear	Linear	Nonlinear	Linear	Nonlinear
Converged	Yes	No	Yes	Yes	$\delta t \downarrow$	$\delta t \downarrow$	Yes	Yes

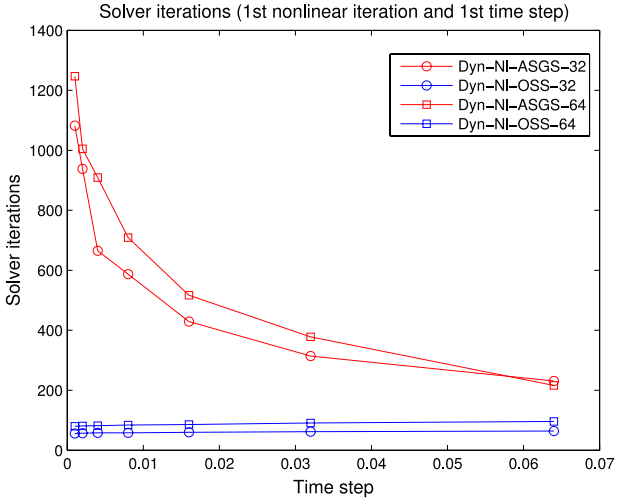

Fig. 18. Solver iterations at the first time step for the DHIT test.

This result is a numerical evidence of the fact that the use of convective terms without the skew-symmetric property produce energy (see also Section 5.2.3) that can make simulations unstable. Further, *these results evidence once again that it is a good choice to stick to provably unconditionally stable formulations, i.e., the dynamic formulations and/or orthogonal subscales formulations with a skew-symmetric convective term*. Similar results have been reported in the finite difference context in [29], where it is shown that stable simulations of the TCF can be performed using an energy-preserving skew-symmetric formulation.

To the best of our knowledge, the stability (or instability) of dynamic ASGS methods has not been proved. In our numerical experiments the static and dynamic linear versions fail to converge in some problems (e.g. DHIT) but we have not found these problems with the Dyn-Nl-ASGS method. Nevertheless, we have found an important increase in the computational cost when the time step is reduced. This behavior is explained in Fig. 18, where the number of solver iterations at the first time step is plotted against the time step size for the dynamic and nonlinear cases of ASGS and OSS methods, with 32^3 and 64^3 $Q1$ mesh, for the DHIT test case. *The number of required solver iterations (and as a result the condition number of the system matrix) blows up exponentially for the ASGS method as we reduce the time step size, whereas it remains constant for the OSS method*. This important observation explains the computational cost trends observed in the previous section.

10. Conclusions

In this paper we have assessed the performance of the numerical formulations previously developed in our group [7,16,22,44] for turbulent incompressible flow problems.

The methods proposed are different to those whose testing in turbulent regimes has been published before, the closest ones being those reported in [18,24]. First, we consider orthogonal subscales formulations. Further, in [18] the ASGS method with quasi-static subscales is used (in the isogeometrical analysis context) but the time step dependency is included in the stabilization parameter (with the inconsistencies and problems discussed in Section 9) and the nonlinear scale splitting is applied in the FE equation only (not in the subscale equation). Time dependent subscales are used in [24], but the authors consider a linear scale splitting. Furthermore, in both works $\tau_c \neq 0$.

First, we have discussed some theoretical aspects, such as the dissipative structure of the methods and the way energy is conserved, which we have numerically verified. Related to this point, we analyze the effect of using different skew-symmetric forms of the convective term, and its impact on energy conservation; if a skew symmetric form is not used, negative energy dissipation can be introduced to the scheme, which may be a source of instability.

However, the most important conclusions come from the different problems that we have solved numerically. Overall, OSS and ASGS yield similar results, all displaying the features of turbulent flows, reproducing appropriately global outputs such as energy spectra. The methods are stable and converge to reference solutions, both when the mesh is refined and when the polynomial order is increased.

On the other hand, we have thoroughly analyzed the effect of the algorithmic constants for isotropic turbulence and wall-bounded turbulent flows, and chosen them based on this sensitivity analysis. An important observation in this line is the fact that all the methods considered in this work are certainly sensitive to the algorithmic constants and they have to be properly chosen in order to simulate turbulent flows on coarse meshes. In fact, the differences in the numerical results are much more influenced by the algorithmic constants than by the choice of the VMS formulation itself. This strong influence seems to be a characteristic feature of turbulence, since in our experience it is not so important in laminar flows. Further, we have analyzed the effect of small time steps when the stabilization parameters depend on them.

Apart from the quality of the results, the OSS method with dynamic subscales is convenient in terms of numerical performance. It requires more nonlinear iterations than ASGS, but less iterations of the linear solver, altogether leading to lower computational cost. In both formulations, ASGS and OSS, the use of dynamic subscales has been found to be crucial for nonlinear convergence. In fact, in some cases quasi-static subscales failed to converge. We have explained these facts by plotting the number of solver iterations required to converge as we reduce the time step size, for a fixed mesh in space. The number of iterations (and as a result the condition number of the system matrix) blows up exponentially for ASGS whereas it remains bounded for OSS.

Acknowledgments

This work has been partially funded by the European Research Council under the FP7 Programme Ideas through the Starting Grant No. 258443—COMFUS: Computational Methods for Fusion Technology. We also acknowledge the financial support received from the Spanish Ministry of Economics and Competitiveness, National Programme of R&D to the project PARANAT (ENE2011-28825). R. Codina gratefully acknowledges the support received from the ICREA Acadèmia Program from the Catalan Government. Furthermore, O. Colomés would like to acknowledge the support received from the Catalan Government through a FI fellowship.

References

[1] P. Sagaut, Large Eddy Simulation for Incompressible Flows, in: Scientific Computing, Springer, 2006.
[2] J.P. Boris, F.F. Grinstein, E.S. Oran, R.L. Kolbe, New insights into large eddy simulation, Fluid Dyn. Res. 10 (4–6) (1992) 199.
[3] C. Fureby, F.F. Grinstein, Large eddy simulation of high-Reynolds-number free and wall-bounded flows, J. Comput. Phys. 181 (1) (2002) 68–97.
[4] F.F. Grinstein, L.G. Margolin, W.J. Rider, Implicit Large Eddy Simulation: Computing Turbulent Fluid Dynamics, Cambridge University Press, 2007.
[5] T.J. Hughes, Multiscale phenomena: Green's functions, the Dirichlet-to-Neumann formulation, subgrid scale models, bubbles and the origins of stabilized methods, Comput. Methods Appl. Mech. Engrg. 127 (1–4) (1995) 387–401.
[6] T.J. Hughes, G.R. Feijóo, L. Mazzei, J.-B. Quincy, The variational multiscale method—a paradigm for computational mechanics, Comput. Methods Appl. Mech. Engrg. 166 (1–2) (1998) 3–24.
[7] J. Principe, R. Codina, F. Henke, The dissipative structure of variational multiscale methods for incompressible flows, Comput. Methods Appl. Mech. Engrg. 199 (13–16) (2010) 791–801.
[8] J. Douglas, J. Wang, An absolutely stabilized finite element method for the Stokes problem, Math. Comp. 52 (1989) 495–508.
[9] T.J.R. Hughes, L.P. Franca, M. Balestra, A new finite element formulation for computational fluid dynamics: V. Circumventing the Babuska–Brezzi condition: a stable Petrov–Galerkin formulation of the Stokes problem accommodating equal-order interpolations, Comput. Methods Appl. Mech. Engrg. 59 (1) (1986) 85–99.
[10] A.N. Brooks, T.J.R. Hughes, Streamline upwind/Petrov–Galerkin formulations for convection dominated flows with particular emphasis on the incompresible Navier–Stokes equations, Comput. Methods Appl. Mech. Engrg. 32 (1982) 199–259.
[11] T.J.R. Hughes, L. Mazzei, K.E. Jansen, Large eddy simulation and the variational multiscale method, Comput. Vis. Sci. 3 (2000) 47–59.
[12] T.J.R. Hughes, A.A. Oberai, L. Mazzei, Large eddy simulation of turbulent channel flows by the variational multiscale method, Phys. Fluids 13 (6) (2001) 1784–1799.

[13] T.J.R. Hughes, L. Mazzei, A.A. Oberai, The multiscale formulation of large eddy simulation: Decay of homogeneous isotropic turbulence, Phys. Fluids 13 (2) (2001) 505–512.
[14] B. Koobus, C. Farhat, A variational multiscale method for the large eddy simulation of compressible turbulent flows on unstructured meshes—application to vortex shedding, Comput. Methods Appl. Mech. Engrg. 193 (15–16) (2004) 1367–1383.
[15] V. John, A. Kindl, Variants of projection-based finite element variational multiscale methods for the simulation of turbulent flows, Internat. J. Numer. Methods Fluids 56 (8) (2008) 1321–1328.
[16] R. Codina, Stabilized finite element approximation of transient incompressible flows using orthogonal subscales, Comput. Methods Appl. Mech. Engrg. 191 (39–40) (2002) 4295–4321.
[17] V. Calo, Residual based mulstiscale turbulence modeling: finite volume simulations of bypass transition (Ph.D. thesis), Department of Civil and Environmental Engineering, Stanford University, 2004.
[18] Y. Bazilevs, V. Calo, J. Cottrell, T. Hughes, A. Reali, G. Scovazzi, Variational multiscale residual-based turbulence modeling for large eddy simulation of incompressible flows, Comput. Methods Appl. Mech. Engrg. 197 (1–4) (2007) 173–201.
[19] X. Nogueira, L. Cueto-Felgueroso, I. Colominas, H. Gómez, Implicit large eddy simulation of non-wall-bounded turbulent flows based on the multiscale properties of a high-order finite volume method, Comput. Methods Appl. Mech. Engrg. 199 (9–12) (2010) 615–624.
[20] T. Hughes, J. Cottrell, Y. Bazilevs, Isogeometric analysis: CAD, finite elements, NURBS, exact geometry and mesh refinement, Comput. Methods Appl. Mech. Engrg. 194 (39–41) (2005) 4135–4195.
[21] R. Codina, Stabilization of incompressibility and convection through orthogonal sub-scales in finite element methods, Comput. Methods Appl. Mech. Engrg. 190 (13–14) (2000) 1579–1599.
[22] R. Codina, J. Principe, O. Guasch, S. Badia, Time dependent subscales in the stabilized finite element approximation of incompressible flow problems, Comput. Methods Appl. Mech. Engrg. 196 (21–24) (2007) 2413–2430.
[23] M. Avila, J. Principe, R. Codina, A finite element dynamical nonlinear subscale approximation for the low Mach number flow equations, J. Comput. Phys. 230 (10–11) (2011) 7988–8009.
[24] P. Gamnitzer, V. Gravemeier, W.A. Wall, Time-dependent subgrid scales in residual-based large eddy simulation of turbulent channel flow, Comput. Methods Appl. Mech. Engrg. 199 (13–16) (2010) 819–827.
[25] S. Badia, J.V. Gutiérrez-Santacreu, Convergence towards weak solutions of the Navier–Stokes equations for a finite element approximation with numerical subgrid scale modeling, IMA J. Numer. Anal. 34 (3) (2014) 1193–1221.
[26] E. Burman, M. Fernández, Galerkin finite element methods with symmetric pressure stabilization for the transient Stokes equations: Stability and convergence analysis, SIAM J. Numer. Anal. 47 (1) (2009) 409–439.
[27] J.-L. Guermond, Faedo–Galerkin weak solutions of the Navier–Stokes equations with Dirichlet boundary conditions are suitable, J. Math. Pures Appl. 88 (1) (2007) 87–106.
[28] A. Arakawa, Computational design for long-term numerical integration of the equations of fluid motion: Two-dimensional incompressible flow. Part I, J. Comput. Phys. 1 (1) (1966) 119–143.
[29] R.W.C.P. Verstappen, A.E.P. Veldman, Symmetry-preserving discretization of turbulent flow, J. Comput. Phys. 187 (1) (2003) 343–368.
[30] G. Gassner, A skew-symmetric discontinuous Galerkin spectral element discretization and its relation to SBP-SAT finite difference methods, SIAM J. Sci. Comput. 35 (3) (2013) A1233–A1253.
[31] F.X. Trias, O. Lehmkuhl, A. Oliva, C.D. Pérez-Segarra, R.W.C.P. Verstappen, Symmetry-preserving discretization of Navier–Stokes equations on collocated unstructured grids, J. Comput. Phys. 258 (2014) 246–267.
[32] D.C. Del Rey Fernández, J.E. Hicken, D.W. Zingg, Review of summation-by-parts operators with simultaneous approximation terms for the numerical solution of partial differential equations, Comput. & Fluids 95 (2014) 171–196.
[33] M. Svärd, J. Nordström, Review of summation-by-parts schemes for initial–boundary-value problems, J. Comput. Phys. 268 (2014) 17–38.
[34] R. Calderer, A. Masud, Residual-based variational multiscale turbulence models for unstructured tetrahedral meshes, Comput. Methods Appl. Mech. Engrg. 254 (2013) 238–253.
[35] V. Gravemeier, M.W. Gee, M. Kronbichler, W.A. Wall, An algebraic variational multiscale-multigrid method for large eddy simulation of turbulent flow, Comput. Methods Appl. Mech. Engrg. 199 (13–16) (2010) 853–864.
[36] A. Masud, R. Calderer, A variational multiscale method for incompressible turbulent flows: Bubble functions and fine scale fields, Comput. Methods Appl. Mech. Engrg. 200 (33–36) (2011) 2577–2593.
[37] R. Temam, Navier Stokes Equations, third ed., in: Studies in Mathematics and its Applications, vol. 2, Elsevier Science, The Netherlands, 1984.
[38] S. Badia, On stabilized finite element methods based on the Scott–Zhang projector. Circumventing the inf–sup condition for the Stokes problem, Comput. Methods Appl. Mech. Engrg. 247–248 (2012) 65–72.
[39] M.-C. Hsu, Y. Bazilevs, V. Calo, T. Tezduyar, T. Hughes, Improving stability of stabilized and multiscale formulations in flow simulations at small time steps, Comput. Methods Appl. Mech. Engrg. 199 (13–16) (2010) 828–840.
[40] D. Fauconnier, C. De Langhe, E. Dick, Construction of explicit and implicit dynamic finite difference schemes and application to the large-eddy simulation of the Taylor–Green vortex, J. Comput. Phys. 228 (21) (2009) 8053–8084.
[41] S. Hickel, N.A. Adams, J.A. Domaradzki, An adaptive local deconvolution method for implicit LES, J. Comput. Phys. 213 (1) (2006) 413–436.
[42] O. Guasch, R. Codina, Statistical behavior of the orthogonal subgrid scale stabilization terms in the finite element large eddy simulation of turbulent flows, Comput. Methods Appl. Mech. Engrg. (2013).
[43] J. Principe, R. Codina, On the stabilization parameter in the subgrid scale approximation of scalar convection–diffusion–reaction equations on distorted meshes, Comput. Methods Appl. Mech. Engrg. 199 (21) (2010) 1386–1402.
[44] R. Codina, J. Principe, S. Badia, Dissipative structure and long term behavior of a finite element approximation of incompressible flows with numerical subgrid scale modeling, in: R. Borst, E. Ramm (Eds.), Multiscale Methods in Computational Mechanics, in: Lecture Notes in Applied and Computational Mechanics, vol. 55, Springer, Netherlands, 2011, pp. 75–93.

[45] S. Badia, R. Codina, On a multiscale approach to the transient Stokes problem: Dynamic subscales and anisotropic space–time discretization, Appl. Math. Comput. 207 (2) (2009) 415–433.
[46] R. Codina, Analysis of a stabilized finite element approximation of the Oseen equations using orthogonal subscales, Appl. Numer. Math. 58 (2008) 264–283.
[47] S. Badia, R. Codina, J.V. Gutiérrez-Santacreu, Long-term stability estimates and existence of a global attractor in a finite element approximation of the Navier–Stokes equations with numerical subgrid scale modeling, SIAM J. Numer. Anal. 48 (3) (2010) 1013–1037.
[48] N.N. Mansour, A.A. Wray, Decay of isotropic turbulence at low Reynolds number, Phys. Fluids 6 (2) (1994) 808–814.
[49] T. Ishida, P.A. Davidson, Y. Kaneda, On the decay of isotropic turbulence, J. Fluid Mech. 564 (2006) 455–475.
[50] Rogallo, Numerical Experiments in Homogeneous Turbulence, in: NASA Technical Memorandum, vol. 81315, 1981.
[51] AGARD-AR-345, A selection of test cases for the validation of large-eddy simulations of turbulent flows. Technical Report, 1998.
[52] S. Badia, A. Martín, J. Principe, Enhanced balancing Neumann–Neumann preconditioning in computational fluid and solid mechanics, Internat. J. Numer. Methods Engrg. 96 (4) (2013) 203–230.
[53] J. Mandel, Balancing domain decomposition, Commun. Numer. Methods Eng. 9 (3) (1993) 233–241.
[54] C.R. Dohrmann, A preconditioner for substructuring based on constrained energy minimization, SIAM J. Sci. Comput. 25 (1) (2003) 246–258.
[55] S. Badia, A.F. Martín, J. Principe, Implementation and scalability analysis of balancing domain decomposition methods, Arch. Comput. Methods Eng. 20 (2013) 239–262.
[56] O. Schenk, K. Gärtner, Solving unsymmetric sparse systems of linear equations with PARDISO, Future Gener. Comput. Syst. 20 (3) (2004) 475–487.
[57] O. Schenk, K. Gärtner, On fast factorization pivoting methods for sparse symmetric indefinite systems, Electron. Trans. Numer. Anal. 23 (2006) 158–179.
[58] G. Gassner, A. Beck, On the accuracy of high-order discretizations for underresolved turbulence simulations, Theor. Comput. Fluid Dyn. 27 (3–4) (2013) 221–237.
[59] A.D. Beck, G.J. Gassner, Numerical simulation of the Taylor–Green vortex at Re = 1600 with the discontinuous Galerkin spectral element method for well-resolved and underresolved scenarios, in: 1st International Workshop on High-Order CFD Methods at the 50th AIAA Aerospace Sciences Meeting, Nashville, TN, 2012.
[60] J.B. Chapelier, M. De La Llave Plata, F. Renac, E. Martin, Final abstract for ONERA Taylor–Green DG participation, 2012.
[61] M.E. Brachet, D.I. Meiron, S.A. Orszag, B.G. Nickel, R.H. Morf, U. Frisch, Small-scale structure of the Taylor–Green vortex, J. Fluid Mech. 130 (1983) 411–452.
[62] J. Gullbrand, F.K. Chow, The effect of numerical errors and turbulence models in large-eddy simulations of channel flow, with and without explicit filtering, J. Fluid Mech. 495 (2003) 323–341.
[63] J. Kim, P. Moin, R. Moser, Turbulence statistics in fully developed channel flow at low Reynolds number, J. Fluid Mech. 177 (1987) 133–166.
[64] R.D. Moser, J. Kim, N.N. Mansour, Direct numerical simulation of turbulent channel flow up to $Re_\tau = 590$, Phys. Fluids 11 (4) (1999) 943–945.
[65] M. Avila, R. Codina, J. Principe, Large eddy simulation of low mach number flows using dynamic and orthogonal subgrid scales, Comput. & Fluids 99 (2014) 44–66.
[66] S.B. Pope, Turbulent Flows, Cambridge University Press, 2000.
[67] F. Ham, F. Lien, A. Strong, A fully conservative second-order finite difference scheme for incompressible flow on nonuniform grids, J. Comput. Phys. 177 (1) (2002) 117–133.
[68] H. Choi, P. Moin, Effects of the computational time step on numerical solutions of turbulent flow, J. Comput. Phys. 113 (1) (1994) 1–4.
[69] G. Comte-Bellot, S. Corrsin, Simple Eulerian time correlation of full-and narrow-band velocity signals in grid-generated, turbulence, J. Fluid Mech. 48 (02) (1971) 273–337.